

Article

# The Phase Relations of the Co-Ni-In Ternary System at 673 K and 873 K and Magnetic Properties of Their Compounds

Tonghan Yang <sup>1,2</sup>, Wei He <sup>1,2,\*</sup>, Guojian Chen <sup>2</sup>, Weijing Zeng <sup>2</sup>, Jinzhi Wang <sup>3</sup>, Lingmin Zeng <sup>2</sup> and Jianlie Liang <sup>4</sup>

<sup>1</sup> College of Chemistry and Chemical Engineering, Guangxi University, Nanning 530004, China; yangthan199@163.com

<sup>2</sup> School of Resources, Environment and Materials and Guangxi Key Laboratory of Processing for Non-ferrous Metallic and Featured Materials, Guangxi University, Nanning 530004, China; chgjxx@163.com (G.C.); zmszengweijing@163.com (W.Z.); lmzeng@gxu.edu.cn (L.Z.)

<sup>3</sup> School of Materials and Chemical Engineering, Ningbo University of Technology, Ningbo 315211, China; wangjz@nbut.edu.cn

<sup>4</sup> School of Science, Guangxi University of Nationalities, Nanning 530006, China; liangjl1971@126.com

\* Correspondence: wei\_he@gxu.edu.cn; Tel.: +86-771-327-5918 or +86-771-323-9406

Received: 10 July 2020; Accepted: 4 September 2020; Published: 9 September 2020



**Abstract:** The phase relationships of the ternary Co-Ni-In system at 673 K and 873 K were investigated by means of powder X-ray diffraction, scanning electron microscopy equipped with energy dispersive spectroscopy, and optical microscopy. Though  $\text{CoIn}_2$  does not exist at 873 K, the ternary solid solution  $\text{Co}_{1-x}\text{Ni}_x\text{In}_2$  exists at both 673 K and 873 K with different composition ranges. The Rietveld refinements were carried out to investigate the crystal structure of  $\text{Co}_{1-x}\text{Ni}_x\text{In}_2$  ( $x = 0.540$ , and  $0.580$ ) and  $\text{Ni}_{2-x}\text{Co}_x\text{In}_3$  ( $x = 0.200$ ). The magnetization dependence of temperature (MT) curves of  $\text{Ni}_{2-x}\text{Co}_x\text{In}_3$  ( $x = 0.200$ ) and  $\text{Co}_{1-x}\text{Ni}_x\text{In}_2$  ( $x = 0.540$ ) are similar to those of the ferromagnetic shape memory alloys Ni-Mn-A (A = Ga, Sn, and In), but do not undergo martensitic transformation. The maximum magnetic entropy changes in  $\text{Ni}_{2-x}\text{Co}_x\text{In}_3$  ( $x = 0.200$ ) and  $\text{Co}_{1-x}\text{Ni}_x\text{In}_2$  ( $x = 0.540$ ) under 3T are 1.25 and 1.475  $\text{J kg}^{-1}\text{K}^{-1}$ , respectively.

**Keywords:** Co-Ni-In; phase diagram; X-ray diffraction; magnetic properties

## 1. Introduction

Recently, Ni-Mn-In has drawn increasing attention due to its fascinating multifunctional properties including its shape memory effect [1], magnetocaloric effect [2], elastocaloric effect [3], magnetothermal conductivity [4], magnetic superelasticity [5], barocaloric effect [6], and large exchange bias effect [7] associated with the martensitic-type phase transformation. A large number of researches have shown that the properties of the Ni-Mn-In alloys have been highly improved when accompanied with a small amount of Co doping into Ni-Mn-In ternary compounds [8–10]. This brings more attention to the Ni-Co-Mn-In quaternary compounds and another upsurge of research of the alloys [11–14]. The martensitic transformation, which belongs to first-order magnetostructural transformation, led to a large magnetic entropy change ( $\Delta S$ ) which makes Ni-Co-Mn-In alloys promising candidates for magnetic refrigeration materials [15–17]. A giant magnetocaloric effect driven by structural transitions was found in  $\text{Ni}_{45.7}\text{Mn}_{36.3}\text{In}_{13}\text{Co}_5$ , which resulted in a high adiabatic temperature change ( $\Delta T_{\text{ad}}$ ) of  $-6.2$  K under a low field of 2T [2]. In Cheng's work, the temperature-induced martensitic transformation of  $\text{Ni}_{42}\text{Co}_8\text{Mn}_{37.7}\text{In}_{12.3}$  alloy achieved a giant ( $\Delta S$ ) of  $14.30 \text{ J}\cdot\text{K}^{-1}\cdot\text{kg}^{-1}$  and refrigeration capacity (RC) up to  $549 \text{ J}\cdot\text{K}^{-1}$ . Additionally, the near-room-temperature working temperature range

of 248–295 K makes it superior among a number of reported magnetocaloric materials [18]. Large magnetic field-induced martensitic transformation led to enormous recoverable deformation, which can be easily observed in Ni-Co-Mn-In alloys, making it an attractive shape memory functional material [19–21]. Stresses of over 100 MPa were generated in  $\text{Ni}_{45}\text{Co}_5\text{Mn}_{36.7}\text{In}_{13.3}$  on the field of 7 T. 3 % deformation, and full recovery of the original shape was discovered as a result of magnetic field-induced strains [1]. After sintering at 873 K,  $\text{Ni}_{45}\text{Mn}_{36.6}\text{In}_{13.4}\text{Co}_5$  showed an almost perfect shape memory effect in which martensitic transformation played the dominant role, since the shape recovery was as high as 11.4% [22]. With such excellent magnetocaloric and shape memory properties, they can extensively serve society. However, large thermal transformation hysteresis, needing a high-driving magnetic field and poor mechanical properties, severely hinders their commercialization [10,23,24]. Phase diagrams are important for designing and preparing of Ni-Co-Mn-In alloys with potentially excellent properties. In addition, they enable the exploration of new functional materials. Only the phase diagrams of the Ni-Mn-In and Ni-Co-Mn ternary systems among the four sub-ternary systems of the Ni-Co-Mn-In quaternary system have been studied [25–28], while the phase diagrams of the other systems are not available in literature. At the same time, investigation on the magnetic properties of the compounds in these three ternary systems also plays a significant role in exploring new potential magnetic materials, such as refrigeration materials. This paper will focus on one of the four sub-ternary systems of the Ni-Co-Mn-In quaternary system, the Co-Ni-In system, and the magnetic properties of its compounds.

The phase diagrams of the binary systems Co-Ni, Co-In, and Ni-In related to the Ni-Co-In ternary system have been studied [29–31]. According to the Co-Ni binary phase diagram, there is no intermediate phase in this system. Co and Ni form an infinite solid solution that exists in the form of  $\alpha$ -(CoNi) (space group:  $\text{Fm}\bar{3}\text{m}$ ) above 695 K. Below 695 K, the alloys are in a  $\epsilon$ -(CoNi) hexagonal phase (Space group  $\text{P6}_3/\text{mm}$ ) at a low nickel content range. With the increase in Ni content, the  $\epsilon$ -Co  $\rightarrow$   $\alpha$ -Co transformation occurs. Two binary compounds,  $\text{CoIn}_2$  and  $\text{CoIn}_3$ , exist in the Co-In binary system, and the compounds are formed by peritectic reactions of  $\alpha$ -Co + L  $\rightarrow$   $\text{CoIn}_2$  (823 K) and  $\text{CoIn}_2$  + L  $\rightarrow$   $\text{CoIn}_3$  (763 K), respectively. The binary system undergoes a monotectic reaction at 1559 K. The composition of the monotectic is about 77 at.% In.

There are seven binary compounds, i.e.,  $\text{Ni}_3\text{In}$ ,  $\text{Ni}_2\text{In}$ ,  $\zeta$ ,  $\text{Ni}_{13}\text{In}_9$ ,  $\text{NiIn}$ ,  $\delta$ ,  $\text{Ni}_2\text{In}_3$ , and  $\text{Ni}_3\text{In}_7$  in the Ni-In binary system according to Ref. [31]. Intermetallic compounds of  $\text{Ni}_3\text{In}$ ,  $\text{Ni}_2\text{In}$ ,  $\text{NiIn}$ ,  $\text{Ni}_2\text{In}_3$ , and  $\text{Ni}_3\text{In}_7$  are stoichiometrically determined. The  $\zeta$  phase is stable from 755 to 1223 K with a maximum range from 31.2 to 40.5 at.% In, and the compound  $\text{Ni}_{13}\text{In}_9$  has a composition range of 38.0–41.0 at.% In, and the compound  $\text{Ni}_{13}\text{In}_9$  have a composition range of 38.0–41.0 at.% In. Additionally, the  $\delta$  phase forming at higher temperature is stable in the temperature range of 1043–1203 K and has a composition range of 52–58.2 at.% In. The solid solubility of In in Ni increases with temperature, which increases from 3.3 to 13.4 at.% In when temperature increases from 693 to 1181 K. No solubility of Ni in In has been reported. A ternary compound,  $\text{Ni}_2\text{CoIn}$ , was investigated theoretically by first principles in [32], showing that the compound crystallized in a cubic structure with a space group of  $\text{Fm}\bar{3}\text{m}$  and lattice parameter  $a = 0.5944$  nm. The Ni atom occupies the 8c (0.25, 0.25, 0.25) site, Co occupies the 4b (0.5, 0.5, 0.5) site, and the In atom occupies the 4a (0, 0, 0) site. Calculation of formation energy indicates the instability of the austenitic structure in  $\text{Ni}_2\text{CoIn}$  and a strong tendency of martensitic transformation. Table 1 shows the crystallographic data of the compounds in the Co-Ni-In system.

**Table 1.** Crystallographic data of the compounds in the Co-Ni-In system.

Compounds	Structure Type	Space Group	Lattice Parameters (nm)				References
			a	b	c	$\beta$ (°)	
CoIn <sub>2</sub>	CuMg <sub>2</sub>	Fddd	0.9402	0.5282	1.7846	90	[30]
CoIn <sub>3</sub>	Mg	P6 <sub>3</sub> /mmc	0.6829	0.6829	0.7094	90	[30]
Ni <sub>4</sub> In	W	Im $\bar{3}$ m	0.2929	0.2929	0.2929	90	[33]
Ni <sub>3</sub> In	Ni <sub>3</sub> Sn	P6 <sub>3</sub> /mmc	0.5320	0.5320	0.4242	90	[31]
Ni <sub>3</sub> In	AuCu <sub>3</sub>	Pm $\bar{3}$ m	0.3750	0.3750	0.3750	90	[31]
$\zeta$	NiAs	P6 <sub>3</sub> /mmc	0.4189	0.4189	0.5123	90	[31]
Ni <sub>2</sub> In	Ni <sub>2</sub> In	P6 <sub>3</sub> /mmc	0.4179	0.4179	0.5131	90	[31]
Ni <sub>13</sub> In <sub>9</sub>	Ni <sub>13</sub> In <sub>9</sub>	C2/m	1.4646	0.8329	0.8977	35.35	[31]
Ni <sub>13</sub> In <sub>7</sub>	AsNi	P6 <sub>3</sub> /mmc	0.4178	0.4178	0.5137	90	[33]
NiIn	CoSn	P6/mmm	0.5243	0.5243	0.4342	90	[31]
NiIn	CsCl	Pm $\bar{3}$ m	0.3092	0.3092	0.3092	90	[31]
Ni <sub>2</sub> In <sub>3</sub>	Al <sub>3</sub> Ni <sub>2</sub>	P $\bar{3}$ m1	0.4390	0.4390	0.5201	90	[31]
Ni <sub>3</sub> In <sub>7</sub>	Cu <sub>5</sub> Zn <sub>8</sub>	I4 $\bar{3}$ m	0.9180	0.9180	0.9180	90	[33]
Ni <sub>2</sub> CoIn	BiF <sub>3</sub>	Fm $\bar{3}$ m	0.5944	0.5944	0.5944	90	[32]

## 2. Experimental

All samples with a mass of 2 g were prepared in an electric arc furnace under argon atmosphere. The purities of initial metals Co, Ni, and In were 99.9 wt. %, 99.99 wt. % and 99.9 wt. %, respectively. The material source is General Research Institute for Nonferrous Metals (Beijing, China). A proper amount of In was added to each samples due to the loss of In. Titanium was used as the oxygen scavenger during the melting process. The samples were melted three times for the purpose of homogeneity of the alloy samples. All the as-cast samples were sealed in evacuated quartz tubes to anneal at higher temperature for further homogenization. The In-rich (> 50 at.% In) alloys were kept at 923 K/673 K for 30 days, while the other alloys homogenized at 1073 K for 20 days. After homogenization annealing, the samples used for the 873 K section were cooled down to 873 K with a cooling rate of 50 K/day and maintained at 873 K for 20 days to reach equilibrium, while those used for the 673 K section were cooled down to 673 K and maintained at 673 K for 20 days. Finally, all the samples were quenched into ice-water mixture.

The X-ray powder diffraction (XRD) data of the Co-Ni-In alloy samples were obtained by using a Rigaku D/max 2500 V powder diffractometer (Cu K $\alpha$ 1 radiation,  $\lambda = 1.54060$  Å; Tokyo, Japan). The powder XRD data for phase analysis were collected in a continuous scanning mode, and those for Rietveld refinement were collected in a step scanned mode with a step size of 0.02°. The high temperature XRD data were collected by using a Bruker D8 advance diffractometer. The Rietveld refinements for some selected samples were carried out by using FullProf programs [34,35]. Scanning electron microscopy (SEM, Hitachi S-3400N or SU8000; Tokyo, Japan) and optical microscopy (Axio Imager A2m, Zeiss, Jena, Germany) were used for microstructure analysis, and energy dispersive analysis (EDS) was applied for the measurements of sample chemical and phase compositions. The samples used for SEM/EDS measurements were corroded with clear water. Magnetic measurements were carried out in the Physical Property Measurement System (PPMS, Quantum Design; San Diego, CA, USA).

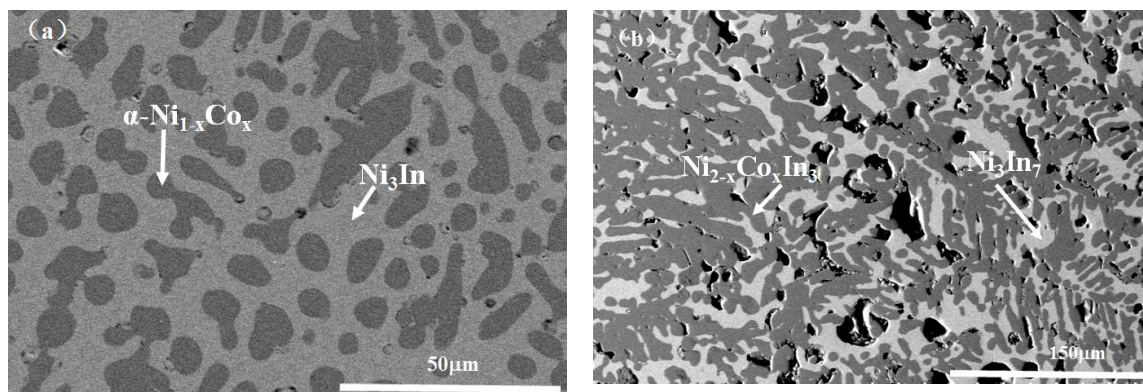
## 3. Results and Discussion

The phase analysis was performed on all the XRD data of the equilibrated Co-Ni-In samples with the aid of the Powder Diffraction File 2 (PDF2) database released by International Center for Diffraction Data (ICDD). The diffraction patterns of those compounds absent in the PDF2 database were calculated from the crystallographic data available in references. By carrying out the phase identification on the XRD patterns of each Co-Ni-In sample, the phase components of each sample were obtained. The selected samples were further observed by SEM/EDS and optical microscopy for phase identification and composition measurements.

### 3.1. Phase Analysis

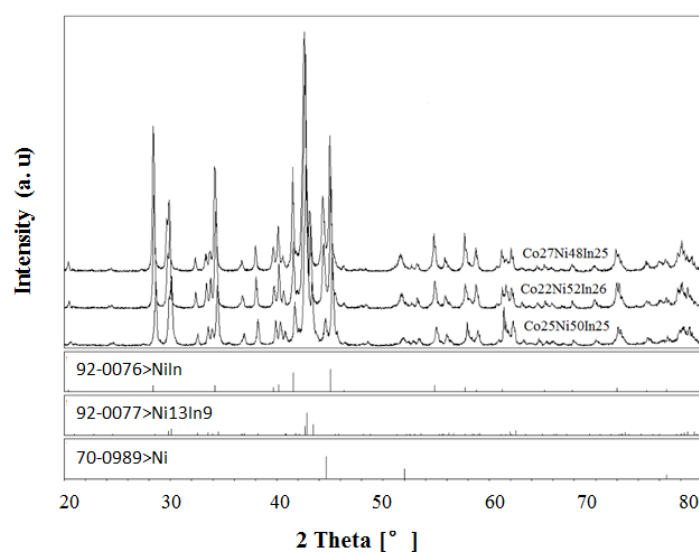
#### 3.1.1. Phase Analysis at 673 K

Table S1 shows the XRD and SEM/EDS analysis results of the selected Co-Ni-In samples at 673 K. The analysis on the XRD patterns of all the binary and ternary Co-Ni-In samples shows eight binary compounds, i.e.,  $\text{Ni}_3\text{In}$ ,  $\text{Ni}_2\text{In}$ ,  $\text{Ni}_{13}\text{In}_9$ ,  $\text{NiIn}$ ,  $\text{Ni}_2\text{In}_3$ ,  $\text{Ni}_3\text{In}_7$ ,  $\text{CoIn}_3$ , and  $\text{CoIn}_2$ , existing at 673 K. The binary compounds  $\text{Ni}_4\text{In}$  and  $\text{Ni}_{13}\text{In}_7$  were not observed in our experimental conditions. This is in good agreement with the Co-Ni, Co-In, and In-Ni binary phase diagrams. The Backscattered electrons (BSE) micrographs of the alloys No. 1 ( $\text{Co}_{10}\text{Ni}_{75}\text{In}_{15}$ ) and No. 2 ( $\text{Co}_4\text{Ni}_{34}\text{In}_{62}$ ) are shown in Figure 1a,b. Both alloys contain two phases. EDS analysis on alloy No. 24 ( $\text{Co}_{10}\text{Ni}_{75}\text{In}_{15}$ ) in Figure 1a revealed that the dark gray phase with composition of  $\text{Co}_{35.53(5)}\text{Ni}_{62.15(4)}\text{In}_{2.31(4)}$  was identified as  $\alpha\text{-NiCo}_x$  ( $x = 0.355$ ), and the gray phase with composition of  $\text{Co}_{1.02(4)}\text{Ni}_{72.26(5)}\text{In}_{26.72(5)}$  was  $\text{Ni}_3\text{In}$ . In Figure 1b, for the sample No. 25 ( $\text{Co}_4\text{Ni}_{34}\text{In}_{62}$ ), the dark gray phase with composition of  $\text{Co}_{2.36(4)}\text{Ni}_{59.12(3)}\text{In}_{38.52(5)}$  was verified to be  $\text{Ni}_{2-x}\text{Co}_x\text{In}_3$  ( $x = 0.118$ ), and the gray phase with composition of  $\text{Co}_{0.86(6)}\text{Ni}_{32.43(5)}\text{In}_{66.72(6)}$  was  $\text{Ni}_3\text{In}_7$ . These results proved the existence of  $\text{Ni}_3\text{In}$ ,  $\text{Ni}_2\text{In}_3$ , and  $\text{Ni}_3\text{In}_7$  at 673 K, which is in agreement with the literature [26,31].



**Figure 1.** BSE micrograph of (a) No. 1 ( $\text{Co}_{10}\text{Ni}_{75}\text{In}_{15}$ ) and (b) No. 2 ( $\text{Co}_4\text{Ni}_{34}\text{In}_{62}$ ).

In order to verify the existence of the ternary compound  $\text{Ni}_2\text{CoIn}$ , which was investigated by using the first principle calculation as described by Bai et al. [35], a series of samples with compositions near  $\text{Ni}_2\text{CoIn}$  was prepared. Figure 2 presents the XRD patterns of sample No. 3 ( $\text{Co}_{25}\text{Ni}_{50}\text{In}_{25}$ ), No. 4 ( $\text{Co}_{22}\text{Ni}_{52}\text{In}_{26}$ ), and No. 5 ( $\text{Co}_{27}\text{Ni}_{48}\text{In}_{25}$ ), and none of the XRD data of these samples correspond to the diffraction pattern calculated from the crystallographic data of  $\text{Ni}_2\text{CoIn}$  as shown in the literature [35]. The XRD analysis on all of these alloys showed that these alloys contained the three phases of  $\text{Ni}_{13-x}\text{Co}_x\text{In}_9$  ( $x = 0.702$ ),  $\text{Ni}_{1-x}\text{Co}_x\text{In}$  ( $x = 0.125$ ), and  $\alpha\text{-Ni}_{1-x}\text{Co}_x$  ( $x = 0.400$ ) pointing to the absence of  $\text{Ni}_2\text{CoIn}$  at 673 K. Figure 3a,b show the SEM micrographs of samples No. 5 and No. 6, respectively, as well as the composition of each phase obtained by EDS. The results also indicated that these two alloys contained the three phases of  $\text{Ni}_{13-x}\text{Co}_x\text{In}_9$  ( $x = 0.702$ ),  $\text{Ni}_{1-x}\text{Co}_x\text{In}$  ( $x = 0.125$ ) and  $\alpha\text{-Ni}_{1-x}\text{Co}_x$  ( $x = 0.4$ ), which proved the non-existence of  $\text{Ni}_2\text{CoIn}$  at 673 K.



**Figure 2.** XRD patterns of samples No. 3 (Co25Ni50In25), No. 4 (Co22Ni52In26), and No. 5 (Co27Ni48In25).

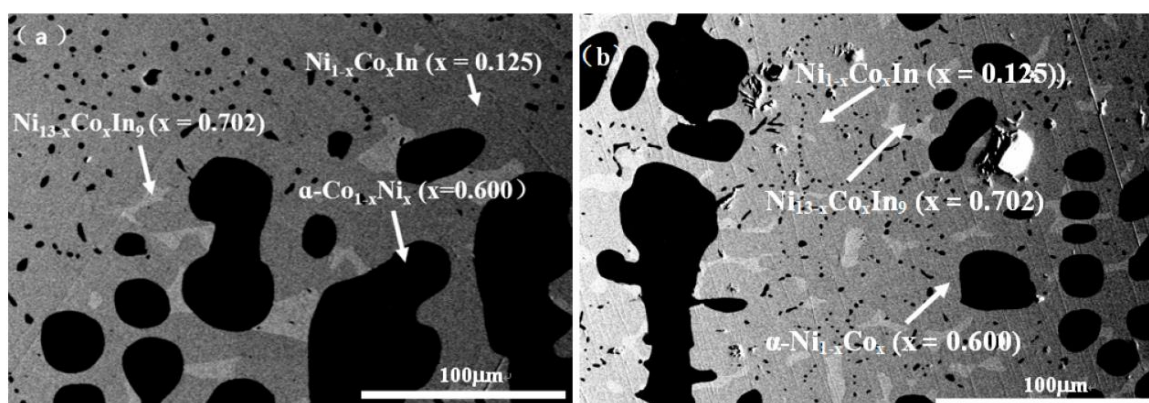


**Figure 3.** BSE micrograph of samples (a) No. 3 (Co25Ni50In25) and (b) No. 4 (Co22Ni52In26).

### 3.1.2. Phase Analysis at 873 K

Table S2 gives the XRD and SEM/EDS analysis results of the selected Co-Ni-In samples at 873 K. The analysis on the XRD patterns of all the binary and ternary Co-Ni-In samples shows that six binary compounds, i.e., Ni<sub>3</sub>In, Ni<sub>2</sub>In, Ni<sub>13</sub>In<sub>9</sub>,  $\xi$ , NiIn, and Co<sub>1-x</sub>Ni<sub>x</sub>In<sub>2</sub>, exist at 873 K.

According to [12], a peritectic reaction  $L + (\alpha) \text{Co} \rightarrow \text{CoIn}_2$  occurs at 823 K, and the compound CoIn<sub>2</sub> does not exist at 873 K. However, in the present work, a solid solution Co<sub>1-x</sub>Ni<sub>x</sub>In<sub>2</sub> was found at 873 K. The solid solution of Co<sub>1-x</sub>Ni<sub>x</sub>In<sub>2</sub> crystallized in the same crystal structure as that of CoIn<sub>2</sub>. Figure 4a,b show the XRD pattern and SEM micrograph of alloy No. 26 (Co28Ni24In48). The XRD analysis result revealed that the alloy contained the three phases of Co<sub>1-x</sub>Ni<sub>x</sub>In<sub>2</sub> ( $x = 0.612$ ), Ni<sub>2-x</sub>Co<sub>x</sub>In<sub>3</sub> ( $x = 0.450$ ), and  $\alpha$ -Co<sub>1-x</sub>Ni<sub>x</sub> ( $x = 0.200$ ), as seen in Figure 4a. The composition measurement showed that the grey phase with composition of Co8.69(5)Ni32.99(4)In58.32(4), the light gray phase with composition of Co20.10(5)Ni16.82(6)In63.08(5), and the dark phase with composition of Co82.21(5)Ni17.16(6)In0.63(5) were identified to be the three phases of Ni<sub>2-x</sub>Co<sub>x</sub>In<sub>3</sub> ( $x = 0.160$ ), Co<sub>1-x</sub>Ni<sub>x</sub>In<sub>2</sub> ( $x = 0.612$ ), and  $\alpha$ -Co<sub>1-x</sub>Ni<sub>x</sub> ( $x = 0.200$ ), respectively, as seen in Figure 4b. Figure 5 shows the XRD pattern of alloy No. 27 (Co26Ni6In68). The XRD pattern in Figure 5 clearly indicates that the alloy contained the two phases of Co<sub>1-x</sub>Ni<sub>x</sub>In<sub>2</sub> and In, which confirmed Co<sub>1-x</sub>Ni<sub>x</sub>In<sub>2</sub> existed at 873 K once again. This suggests that the addition of Ni into CoIn<sub>2</sub> stabilized the compound and raised the temperature of the peritectic reaction  $L + (\alpha) \text{Co} \rightarrow \text{Co}_{1-x}\text{Ni}_x\text{In}_2$ .

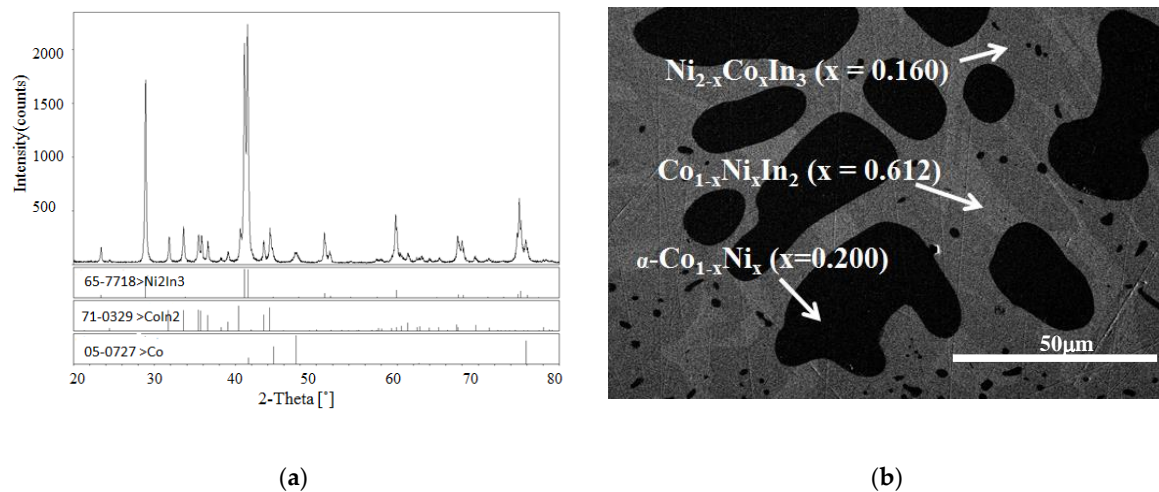


Figure 4. (a) XRD pattern and (b) BSE micrograph of No. 26 (Co<sub>28</sub>Ni<sub>24</sub>In<sub>48</sub>).

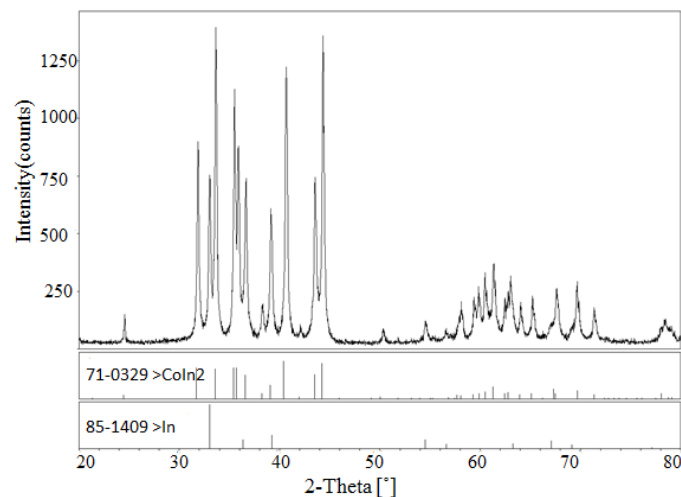


Figure 5. XRD pattern of No.33 (Co<sub>26</sub>Ni<sub>6</sub>In<sub>68</sub>).

The XRD pattern and SEM micrograph of alloy No. 28 (Co<sub>8</sub>Ni<sub>22</sub>In<sub>70</sub>) are shown in Figure 6a,b, respectively. The XRD analysis of the alloy indicated that the three phases of Co<sub>1-x</sub>Ni<sub>x</sub>In<sub>2</sub> (x = 0.612), Ni<sub>2-x</sub>Co<sub>x</sub>In<sub>3</sub> (x = 0.450) and In (Liquid) coexisted in the alloy, and no diffraction patterns of Ni<sub>3</sub>In<sub>7</sub> and/or CoIn<sub>3</sub> were observed. The SEM/EDS analysis on alloy No.28 also gave the same results. This indicates that Ni<sub>3</sub>In<sub>7</sub> and CoIn<sub>3</sub> do not exist at 873 K. Figure 7 shows the SEM micrograph of No. 29 (Co<sub>18</sub>Ni<sub>52</sub>In<sub>30</sub>) alloy. It is clearly seen that the alloy is composed of three phases. EDS measurements showed that the gray phase with composition of Co<sub>10.91(5)</sub>Ni<sub>46.53(4)</sub>In<sub>42.56(4)</sub> was identified as Ni<sub>13-x</sub>Co<sub>x</sub>In<sub>9</sub> (x = 2.634), the dark gray phase with composition of Co<sub>5.94(6)</sub>Ni<sub>55.83(5)</sub>In<sub>38.28(5)</sub> was verified to be ξ, and the dark phase with composition of Co<sub>48.69(4)</sub>Ni<sub>49.12(4)</sub>In<sub>2.19(3)</sub> was α-Ni<sub>1-x</sub>Co<sub>x</sub> (x = 0.500). This result suggests that the ξ phase existed at 873 K, which is similar to Schmetterer's investigation [36].

Compared to the phases at 673 K, the binary compounds, i.e., Ni<sub>3</sub>In, Ni<sub>2</sub>In, Ni<sub>13</sub>In<sub>9</sub>, NiIn, Ni<sub>2</sub>In<sub>3</sub>, and ξ, exist at 873 K, while the binary compounds Ni<sub>3</sub>In<sub>7</sub>, CoIn<sub>3</sub>, and CoIn<sub>2</sub> disappeared at 873 K. Although CoIn<sub>2</sub> does not exist at 873 K, the ternary solid solution Co<sub>1-x</sub>Ni<sub>x</sub>In<sub>2</sub> exists at both of 673 K and 873 K with different composition ranges. No new binary and ternary compounds were found at 673 K and 873 K.

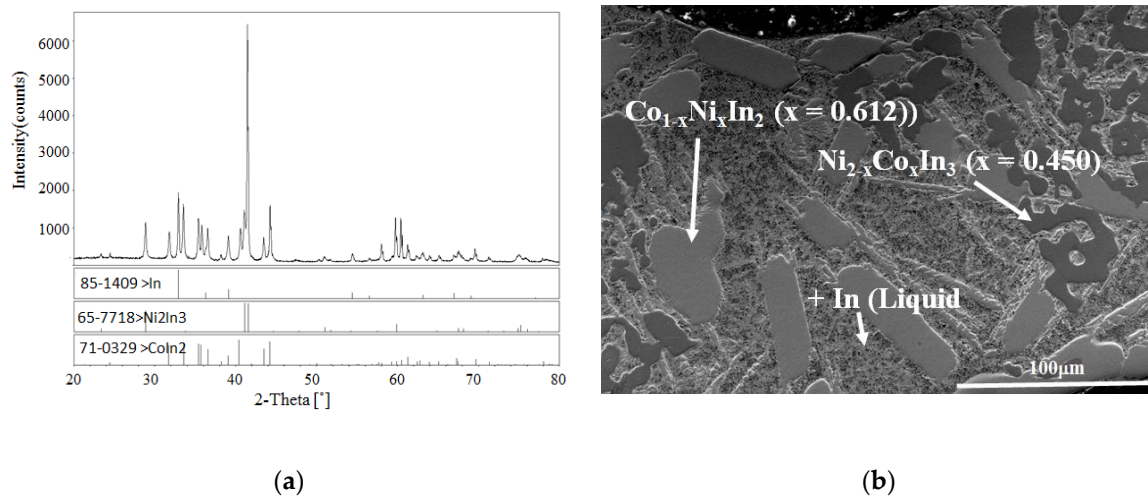


Figure 6. (a) XRD pattern and (b) BSE micrograph of No. 32 ( $\text{Co}_8\text{Ni}_{22}\text{In}_{70}$ ).

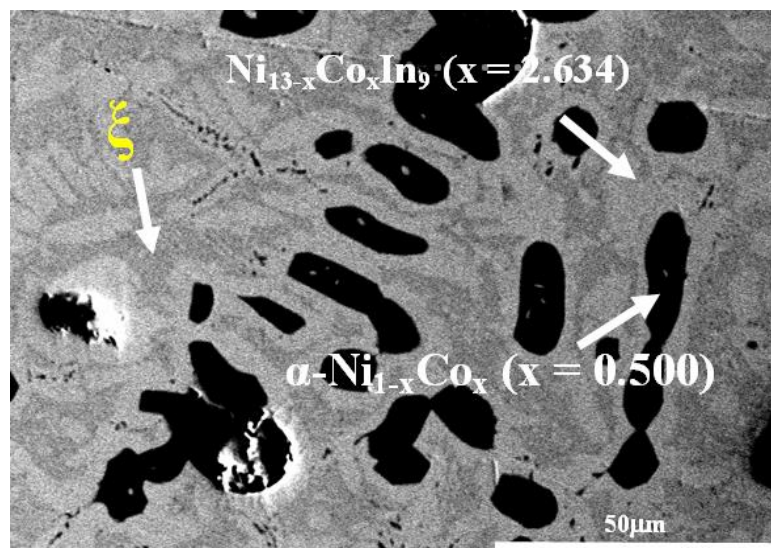


Figure 7. BSE micrograph of No. 28 ( $\text{Co}_{18}\text{Ni}_{52}\text{In}_{30}$ ).

### 3.2. Solid Solubility

The solid solubilities of Co in  $\text{Ni}_2\text{In}$ ,  $\text{NiIn}$ ,  $\text{Ni}_{13}\text{In}_9$ ,  $\text{Ni}_2\text{In}_3$ , and Ni, as well as Ni in  $\text{CoIn}_2$  and Co at 673 K and 873 K were determined by XRD using the phase-disappearing and lattice parameter method combined with the SEM (EDS). The rough maximum solid solubility of above compounds was estimated by comparing the movement of the diffraction patterns of the single phases to the disappearance of the phases. A few series samples such as  $\text{Ni}_{1-x}\text{Co}_x\text{In}$  and  $\text{Co}_{1-x}\text{Ni}_x\text{In}_2$  were prepared for the purpose of the solid solubility determination in the Co-Ni-In ternary system. The computer software Jade 5.0 was used to calculate and refine the lattice parameters of the samples  $\text{Ni}_{1-x}\text{Co}_x\text{In}$  and  $\text{Co}_{1-x}\text{Ni}_x\text{In}_2$  from the XRD patterns.

#### 3.2.1. Solid Solubility at 673 K

Figure 8 presents the XRD patterns of the samples  $\text{Ni}_{1-x}\text{Co}_x\text{In}$  ( $x = 0.04, 0.08, 0.12, 0.14$ ) at 673 K. It can be clearly seen that these samples (except that of  $x = 0.14$ ) contained the single phase of  $\text{Ni}_{1-x}\text{Co}_x\text{In}$ , pointing to the maximum solid solubility of Co in NiIn being between  $x = 0.12$  and  $x = 0.14$ . Figure 9a,b show the variation in the lattice parameter  $a$  and the lattice parameter  $c$  of  $\text{Ni}_{1-x}\text{Co}_x\text{In}$  with the content of Co, which were calculated from the XRD patterns by Jade 5.0. It can be seen from

Figure 9a,b that the maximum solid solubility of Co in  $\text{Ni}_{1-x}\text{Co}_x\text{In}$  is  $x = 0.125$  (6.25 at.% Co). Further analysis on the sample  $\text{Ni}_{1-x}\text{Co}_x\text{In}$  ( $x = 0.14$ ) by the SEM (EDS) also showed that the alloy contains the three phases of  $\text{Ni}_{1-x}\text{Co}_x\text{In}$  ( $x = 0.125$ ),  $\text{Ni}_{2-x}\text{Co}_x\text{In}_3$  ( $x = 0.400$ ), and  $\varepsilon\text{-Co}_{1-x}\text{Ni}_x$  ( $x = 0.280$ ), as seen in Figure 10, which is felt in a three-phase region. The composition measurement shows that the dark grey phase with composition of  $\text{Co}5.75(5)\text{Ni}45.02(6)\text{In}49.23(6)$  is  $\text{Ni}_{1-x}\text{Co}_x\text{In}$  ( $x = 0.125$ ), the grey phase with composition of  $\text{Co}7.82(4)\text{Ni}33.11(5)\text{In}58.07(5)$  is  $\text{Ni}_{2-x}\text{Co}_x\text{In}_3$  ( $x = 0.400$ ) and the dark phase with composition of  $\text{Co}72.81(7)\text{Ni}26.18(6)\text{In}1.01(5)$  is  $\varepsilon\text{-Co}_{1-x}\text{Ni}_x$  ( $x = 0.280$ ). This caused the maximum solid solubility of Co in  $\text{Ni}_{1-x}\text{Co}_x\text{In}$  to be 5.82 at.% Co at 673 K, and this value is similar to that obtained by the lattice parameter method, i.e.,  $x = 0.125$  (6.25 at.% Co). This further supports that the maximum solid solubility of Co in  $\text{Ni}_{1-x}\text{Co}_x\text{In}$  is 6.25 at.% Co at 673 K.

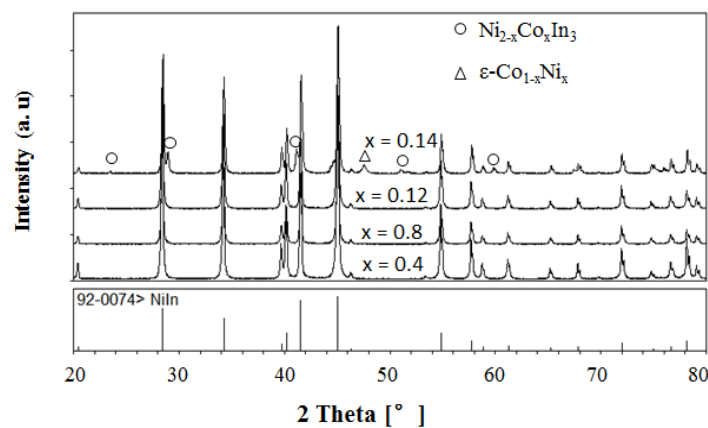


Figure 8. XRD patterns of the sample  $\text{Ni}_{1-x}\text{Co}_x\text{In}$  ( $x = 0.04, 0.08, 0.12, 0.14$ ).

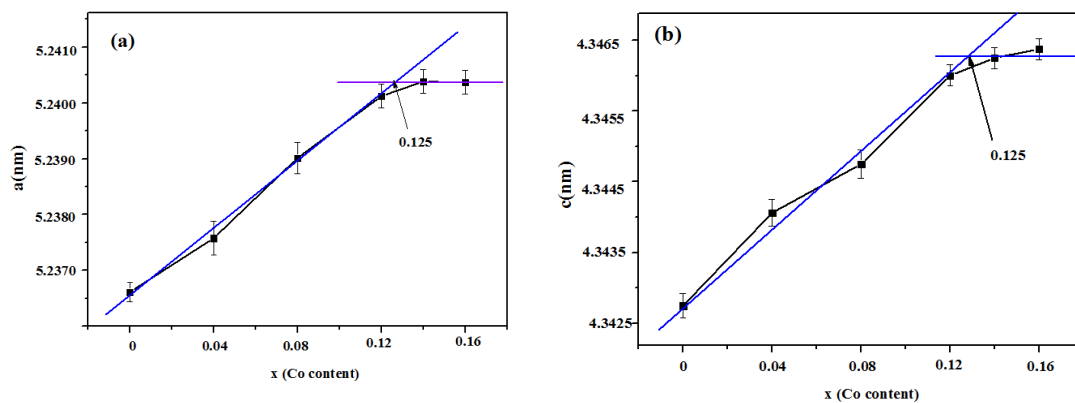


Figure 9. Variation of (a) the lattice parameter  $a$  and (b) lattice parameter  $c$  of  $\text{Ni}_{1-x}\text{Co}_x\text{In}$  on Co content.

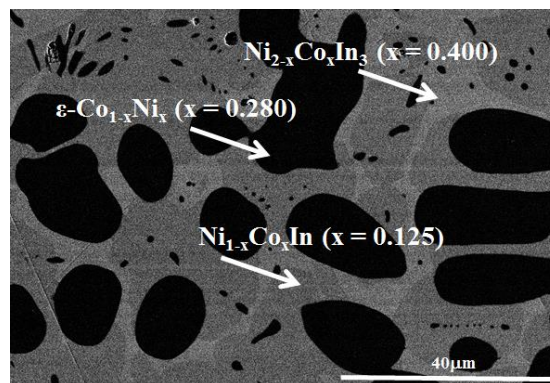
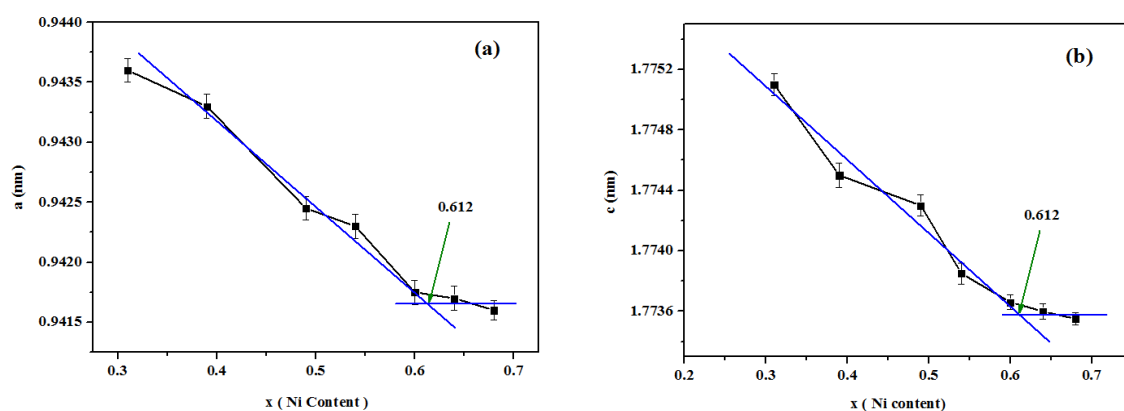


Figure 10. BSE micrograph of the sample  $\text{Ni}_{1-x}\text{Co}_x\text{In}$  ( $x = 0.14$ ).

Similarly, the maximum solid solubilities of Ni in  $\text{Co}_{1-x}\text{Ni}_x\text{In}_2$  and  $\varepsilon\text{-Co}_{1-x}\text{Ni}_x$  were determined to be 18.64 and 28 at.% Ni at 673 K, respectively. The maximum solid solubilities of Co in  $\text{Ni}_{2-x}\text{Co}_x\text{In}$ ,  $\text{Ni}_{13-x}\text{Co}_x\text{In}_9$ ,  $\text{Ni}_{2-x}\text{Co}_x\text{In}_3$ , and  $\alpha\text{-Ni}_{1-x}\text{Co}_x$  were about 3, 3.2, 8, and 60 at.% Co at 673 K.

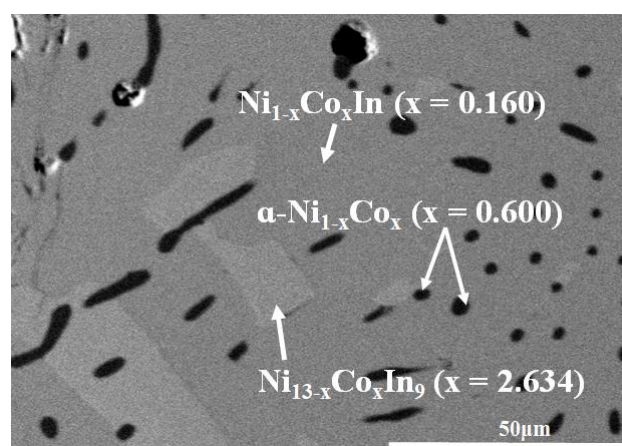
### 3.2.2. Solid Solubility at 873 K

Figure 11a,b show the variation of the lattice parameter  $a$  and the lattice parameter  $c$  of  $\text{Co}_{1-x}\text{Ni}_x\text{In}_2$  with the content of Ni, which indicated that the maximum solid solubility of Ni in  $\text{Co}_{1-x}\text{Ni}_x\text{In}_2$  is  $x = 0.612$  (about 20.19 at.% Co). The SEM micrograph of No. 26 is given in Figure 4b. The composition measurement of the light grey phase with composition of  $\text{Co}_{20.10(5)}\text{Ni}_{16.82(5)}\text{In}_{63.08(5)}$ , which was  $\text{Co}_{1-x}\text{Ni}_x\text{In}_2$  ( $x = 0.612$ ), suggested that the maximum solid solubility of Co in  $\text{Co}_{1-x}\text{Ni}_x\text{In}_2$  was 20.1 at.% Co at 873 K. These two values are close. Although the binary  $\text{CoIn}_2$  is absent at 873 K, the addition of Ni in  $\text{CoIn}_2$  stabilized the compounds and kept the solid solution  $\text{Co}_{1-x}\text{Ni}_x\text{In}_2$  with a wide range appeared at 873 K. The solid solubility range of  $\text{Co}_{1-x}\text{Ni}_x\text{In}_2$  is 3–20.1 at.% Co at 873 K.



**Figure 11.** Variation of (a) the lattice parameter  $a$  and (b) lattice parameter  $c$  of  $\text{Co}_{1-x}\text{Ni}_x\text{In}_2$  on Ni content.

The SEM micrograph of alloy No. 30 ( $\text{Co}_{25}\text{Ni}_{45}\text{In}_{35}$ ) in Figure 12 clearly shows that the alloy contains three phases. Further composition measurements indicated that the grey phase with composition of  $\text{Co}_{7.43(5)}\text{Ni}_{43.56(6)}\text{In}_{49.01(6)}$  was confirmed as  $\text{Ni}_{1-x}\text{Co}_x\text{In}$  ( $x = 0.160$ ), the light grey phase with composition of  $\text{Co}_{12.03(6)}\text{Ni}_{47.28(7)}\text{In}_{40.69(6)}$  was verified to be  $\text{Ni}_{13-x}\text{Co}_x\text{In}_9$  ( $x = 2.634$ ) and the dark phase with composition of  $\text{Co}_{61.21(5)}\text{Ni}_{37.51(5)}\text{In}_{1.28(5)}$  was  $\alpha\text{-Ni}_{1-x}\text{Co}_x$  ( $x = 0.600$ ). This further suggests that the maximum solid solubility of Co in  $\text{Ni}_{13-x}\text{Co}_x\text{In}_9$  is about 12.03 at.% Co at 873 K.



**Figure 12.** The BSE micrograph of No. 30 ( $\text{Co}_{25}\text{Ni}_{45}\text{In}_{35}$ ).

Similarly, the maximum solid solubilities of Co in  $Ni_{2-x}Co_xIn$ ,  $Ni_{13-x}Co_xIn_9$ ,  $Ni_{1-x}Co_xIn$ ,  $Ni_{2-x}Co_xIn_3$ , and  $\alpha-Ni_{1-x}Co_x$  were found to be about 6, 12.03, 8, 9, and 60 at.% Co at 873 K, respectively. Both of the maximum solid solubilities of In in  $\epsilon-Co_{1-x}Ni_x$  and  $\alpha-Ni_{1-x}Co_x$  were observed to be less than 3 at.% In.

Clearly, temperature has a great effect on the solid solubility of the third element in the binary compounds of the Co-Ni-In ternary system. Normally, the maximum solid solubilities of the third element increase with the increasing temperature. For example, the maximum solid solubilities of Co in  $Ni_{13-x}Co_xIn_9$  increased from 3.2 at.% Co at 673 K to 12.03 at.% Co at 873 K. However, the solid solubility range of  $Co_{1-x}Ni_xIn_2$  was found to be 0–18.64% at. % Ni 673 K, while it shifted to the range of 3–20.1% at. % Ni at 873 K due to the absence of  $CoIn_2$  at 873 K.

### 3.3. Isothermal Sections of the Co-Ni-In Ternary System at 673 K and 873 K

By comparing and analyzing more than 33 alloy samples of the Co-Ni-In ternary system and identifying the phases presented in each sample by XRD, optical microscopy, and SEM/EDS, the isothermal sections of the phase diagrams of the Co-Ni-In ternary system at 673 K and 873 K were determined. As shown in Figure 13, the isothermal section at 673 K consists of 11 single-phase regions, 21 two-phase regions, and 9 three-phase regions. The typical alloys and the details of the three-phase regions of the isothermal section of the Co-Ni-In ternary system are given in Table 2.

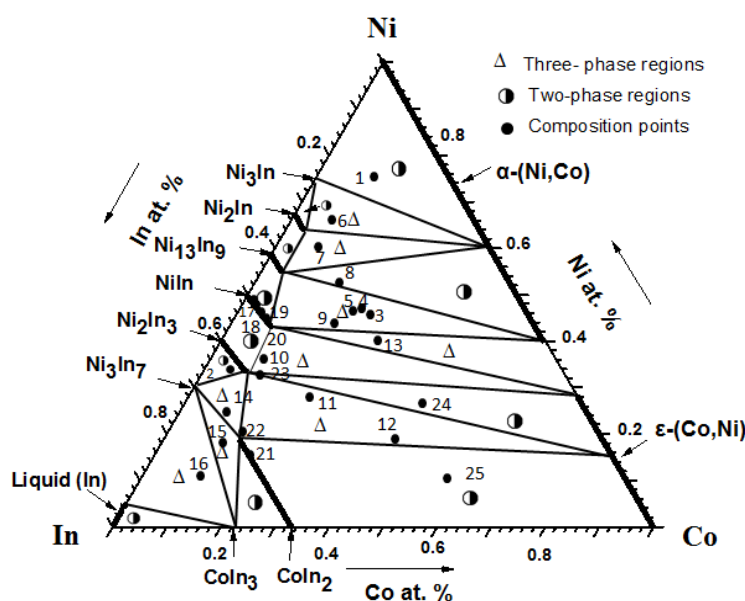


Figure 13. Isothermal section of the Co-Ni-In system at 673 K.

Table 2. Typical samples and details of three-phase regions in the Co-Ni-In ternary system at 673 K.

Phase Regions	Samples	Alloy Compositions	Phase Components
1	No. 6	Co10Ni68In22	$Ni_{2-x}Co_xIn(x = 0.091) + Ni_3In + \alpha-Ni_{1-x}Co_x(x = 0.400)$
2	No. 7	Co10Ni62In28	$Ni_{13-x}Co_xIn_9(x = 0.702) + Ni_{2-x}Co_xIn(x = 0.091) + \alpha-Ni_{1-x}Co_x(x = 0.400)$
3	No. 9	Co20Ni45In35	$Ni_{13-x}Co_xIn_9(x = 0.702) + Ni_{1-x}Co_xIn(x = 0.125) + \alpha-Co_{1-x}Ni_x(x = 0.600)$
4	No. 10	Co10Ni40In50	$Ni_{1-x}Co_xIn(x = 0.125) + Ni_{2-x}Co_xIn_3(x = 0.400) + \epsilon-Co_{1-x}Ni_x(x = 0.280)$
5	No. 11	Co40Ni20In40	$Co_{1-x}Ni_xIn_2(x = 0.565) + Ni_{2-x}Co_xIn_3(x = 0.400) + \epsilon-Co_{1-x}Ni_x(x = 0.280)$
6	No. 13	Co30Ni40In30	$Ni_{1-x}Co_xIn(x = 0.125) + \alpha-Co_{1-x}Ni_x(x = 0.600) + \epsilon-Co_{1-x}Ni_x(x = 0.280)$
7	No. 14	Co10Ni24In66	$Co_{1-x}Ni_xIn_2(x = 0.565) + Ni_{2-x}Co_xIn_3(x = 0.400) + Ni_3In_7$
8	No. 15	Co16Ni12In72	$Co_{1-x}Ni_xIn_2(x = 0.565) + CoIn_3 + Ni_3In_7$
9	No. 16	Co10Ni12In78	$CoIn_3 + Ni_3In_7 + In(Liquid)$

As shown in Figure 14, the isothermal section at 873 K contains 8 single-phase regions, 16 two-phase regions, and 8 three-phase regions. The typical alloys and the details of the three-phase regions of the Co-Ni-In isothermal section at 873 K are presented in Table 3.

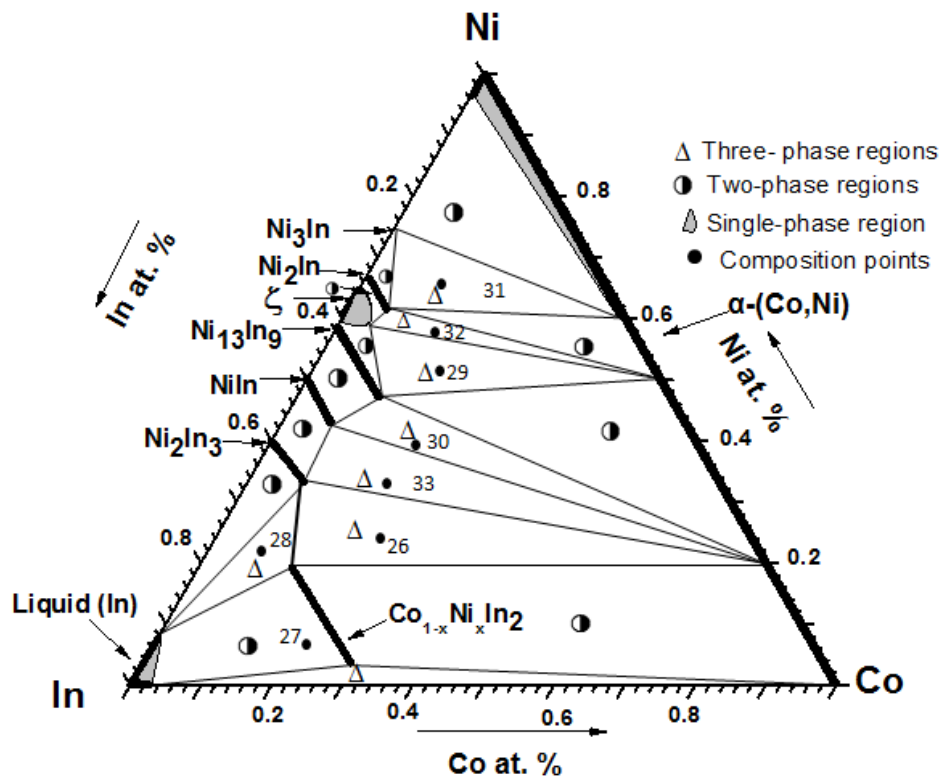


Figure 14. Isothermal section of the Co-Ni-In system at 873 K.

Table 3. Typical samples and details of three-phase regions in the Co-Ni-In ternary system at 873 K.

Phase Regions	Samples	Alloy Compositions	Phase Components
I	No. 26	Co28Ni24In48	$Co_{1-x}Ni_xIn_2$ ( $x = 0.612$ ) + $Ni_{2-x}Co_xIn_3$ ( $x = 0.450$ ) + $\alpha-Co_{1-x}Ni_x$ ( $x = 0.200$ )
II	No. 28	Co8Ni22In70	$Co_{1-x}Ni_xIn_2$ ( $x = 0.612$ ) + $Ni_{2-x}Co_xIn_3$ ( $x = 0.450$ ) + In (Liquid)
III	No. 28	Co18Ni52In30	$\xi + Ni_{13-x}Co_xIn_9$ ( $x = 2.634$ ) + $\alpha-Ni_{1-x}Co_x$ ( $x = 0.500$ )
IV	No. 30	Co20Ni45In35	$Ni_{13-x}Co_xIn_9$ ( $x = 2.634$ ) + $Ni_{1-x}Co_xIn$ ( $x = 0.160$ ) + $\alpha-Ni_{1-x}Co_x$ ( $x = 0.600$ )
V	No. 31	Co14Ni66In20	$Ni_3In + Ni_{2-x}Co_xIn$ ( $x = 0.181$ ) + $\alpha-Ni_{1-x}Co_x$ ( $x = 0.400$ )
VI	No. 32	Co12Ni58In30	$Ni_{2-x}Co_xIn$ ( $x = 0.181$ ) + $\xi + \alpha-Ni_{1-x}Co_x$ ( $x = 0.500$ )
VII	No. 33	Co20Ni34In46	$Ni_{1-x}Co_xIn$ ( $x = 0.160$ ) + $Ni_{2-x}Co_xIn_3$ ( $x = 0.450$ ) + $\alpha-Co_{1-x}Ni_x$ ( $x = 0.200$ )
VIII			$Co_{1-x}Ni_xIn_2$ ( $x = 0.091$ ) + $\alpha-Co + In$ (Liquid)

By comparing the isothermal sections at 673 K and 873 K of phase diagram of the Co-Ni-In ternary system, the differences between the two sections can be found. The three three-phase regions, i.e.,  $Co_{1-x}Ni_xIn_2$  ( $x = 0.565$ ) +  $Ni_{2-x}Co_xIn_3$  ( $x = 0.4$ ) +  $Ni_3In_7$ ,  $Co_{1-x}Ni_xIn_2$  ( $x = 0.565$ ) +  $CoIn_3$  +  $Ni_3In_7$  and  $CoIn_3$  +  $Ni_3In_7$  + In (Liquid) disappear due to the absence of the binary compounds  $Ni_3In_7$  and  $CoIn_3$  at 873 K [12,13], as seen Figure 4. The three-phase region  $Ni_{13-x}Co_xIn_9$  ( $x = 0.702$ ) +  $Ni_{1-x}Co_xIn_2$  ( $x = 0.091$ ) +  $\alpha-Ni_{1-x}Co_x$  ( $x = 0.400$ ) breaks into two three-phase regions, i.e.,  $Ni_{2-x}Co_xIn$  ( $x = 0.181$ ) +  $\xi + \alpha-Ni_{1-x}Co_x$  ( $x = 0.500$ ), and  $\xi + Ni_{13-x}Co_xIn_9$  ( $x = 2.634$ ) +  $\alpha-Ni_{1-x}Co_x$  ( $x = 0.500$ ) since the  $\xi$  phase exist from 746 K to 1223 K [13]. According to the Co-Ni binary phase diagram, the crystal structures of  $Co_{1-x}Ni_x$  alloys belong to the hexagonal structure when the concentration of Ni is less than 10 at.% Ni at 673 K, while its structure starts to change from a hexagonal structure into a cubic structure when Ni content exceed 10 at.% Ni. However, the  $Co_{1-x}Ni_x$  alloy only crystallizes in a cubic structure at 873 K. Therefore, the three-phase region  $Ni_{1-x}Co_xIn$  ( $x = 0.125$ ) +  $\alpha-Co_{1-x}Ni_x$  ( $x = 0.600$ ) +  $\epsilon-Co_{1-x}Ni_x$  ( $x = 0.280$ ) at 673 K becomes a two-phase region,  $Ni_{1-x}Co_xIn$  ( $x = 0.160$ ) +  $\alpha-Ni_{1-x}Co_x$  at 873 K. Although the binary compound  $CoIn_2$  does not exist at 873 K, a narrow three-phase region,  $Co_{1-x}Ni_xIn_2$  ( $x = 0.091$ ) +  $\alpha-Co + In$  (Liquid), presents at 873 K due to the solid solution of  $Co_{1-x}Ni_xIn_2$  ( $x = 0.091-0.612$ ) appearing at 873 K.

### 3.4. Crystal Structure

#### 3.4.1. Crystal Structure of $\text{Ni}_{2-x}\text{Co}_x\text{In}_3$ ( $x = 0.200$ )

The XRD and SEM/EDS data for the sample  $\text{Ni}_{2-x}\text{Co}_x\text{In}_3$  ( $x = 0.200$ ) were collected in order to investigate its crystal structure. The XRD phase analysis points out that this sample is a single phase without any detectable impurity or additional phases. The SEM/EDS testing result shows that the composition of the sample is  $\text{Ni}_{34.62(3)}\text{Co}_{5.23(4)}\text{In}_{60.15(3)}$ , which reveals that 5.23(4)at.% of Co replaces the Ni position in  $\text{Ni}_{2-x}\text{Co}_x\text{In}_3$  ( $x = 0.200$ ). To determine the crystal structures of the  $\text{Ni}_{2-x}\text{Co}_x\text{In}_3$  ( $x = 0.200$ ) alloy, Rietveld refinement was performed from the XRD data by using the FullProf program. The powder X-ray diffraction pattern for the  $\text{Ni}_{2-x}\text{Co}_x\text{In}_3$  ( $x = 0.200$ ) alloy is shown in Figure 15. The Rietveld refinement results of the alloys are listed in Table 4. The low values of the  $R_p$  and  $R_{wp}$  factors suggest that the fitted pattern is in good agreement with the experimental data and that the Rietveld refinement is reliable. The Rietveld refinement results support the case that the structure of sample remains unchanged at room temperature when cobalt is doped into the  $\text{Ni}_{2-x}\text{Co}_x\text{In}_3$  ( $x = 0.200$ ) compound, and  $\text{Ni}_{2-x}\text{Co}_x\text{In}_3$  ( $x = 0.200$ ) crystallizes in the  $\text{Al}_2\text{Ni}_3$ -type structure (space group  $P\bar{3}m1$ ). The lattice parameters are  $a = 0.43959(5)$  nm,  $c = 0.53121(1)$  nm, and  $Z = 1$ . All positions are fully occupied in the compound. The Wyckoff 1a (0, 0, 0) site and 2d (1/3, 2/3, 0.3534 (3)) site are all occupied by In atoms, while the 2d (1/3, 2/3, 0.1381 (2)) site is occupied by Co and Ni atoms (0.1Co + 0.9 Ni).

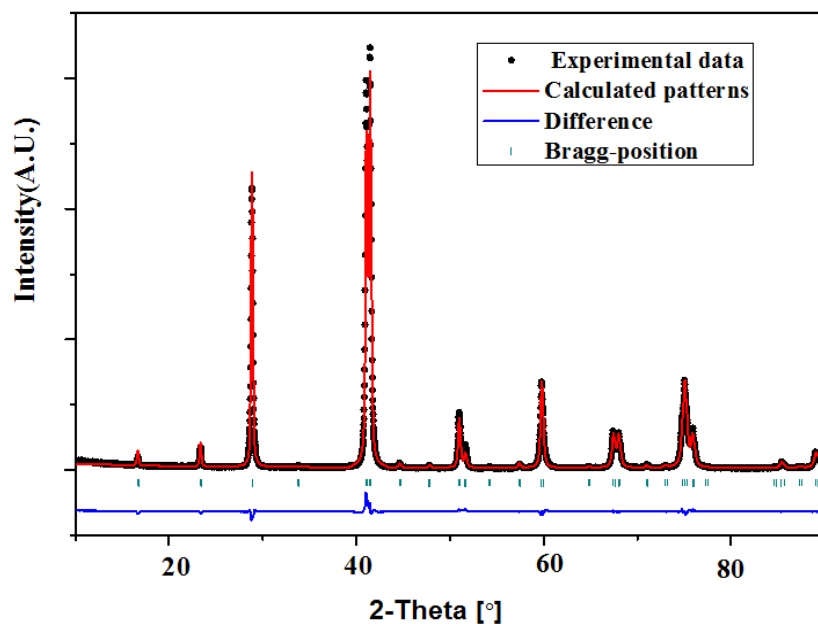


Figure 15. Observed, calculated, and differential XRD patterns of  $\text{Ni}_{2-x}\text{Co}_x\text{In}_3$  ( $x = 0.200$ ).

**Table 4.** Crystallographic data and Rietveld refinement results for Ni<sub>2-x</sub>Co<sub>x</sub>In<sub>3</sub> (x = 0.200) and Co<sub>1-x</sub>Ni<sub>x</sub>In<sub>2</sub> (x = 0.54, 0.58) alloys.

Compound	Phase	Structure Type	Space Group	Lattice Parameters (nm)			Atomic Parameters			Reliability Factors		Goodness of Fit
				a	b	c	Atoms	Wyck (x, y, z)	Occ	R <sub>p</sub> (%)	R <sub>exp</sub> (%)	
Ni <sub>2-x</sub> Co <sub>x</sub> In <sub>3</sub> (x = 0.200)	Ni <sub>2-x</sub> Co <sub>x</sub> In <sub>3</sub> (x = 0.200)	Al <sub>2</sub> Ni <sub>3</sub>	P $\bar{3}$ m1 (164)	0.43959(5)	0.43959(5)	0.53121(1)	In1	1a (0,0,0)	1	10.46	14.15	3.2
							In2	2d (1/3, 2/3, 0.6469(3))	1			
Co <sub>1-x</sub> Ni <sub>x</sub> In <sub>2</sub> (x = 0.540)	Co <sub>1-x</sub> Ni <sub>x</sub> In <sub>2</sub> (x = 0.540)	CuMg <sub>2</sub>	Fddd (70)	0.9424(3)	0.5288(4)	1.7742(5)	M1 = (Co, Ni)	2d (0, 0, 0.1381(2))	0.1Co + 0.9 Ni	10.29	13.26	2.9
							In1	16e (0.9648(2), 1/4, 1/4)	1			
Co <sub>1-x</sub> Ni <sub>x</sub> In <sub>2</sub> (x = 0.580)	Co <sub>1-x</sub> Ni <sub>x</sub> In <sub>2</sub> (x = 0.565)	CuMg <sub>2</sub>	Fddd (70)	0.9421(2)	0.5282(3)	1.7739(3)	M2 = (Co, Ni)	16g (1/4, 0.9963(7), 1/4)	0.466Co + 0.534Ni	9.89	12.58	2.7
							In1	16e (0.9642(3), 1/4, 1/4)	1			
	Ni <sub>2-x</sub> Co <sub>x</sub> In <sub>3</sub> (x = 0.400)	Al <sub>3</sub> Ni <sub>2</sub>	P $\bar{3}$ m1 (164)	0.4397(1)	0.4397(1)	0.5319(3)	In2	16g (1/4, 0.9962(2), 1/4)	1	9.89	12.58	2.7
							In1	1a (0 0 0)	1			
							M4 = (Co, Ni)	2d (1/3, 2/3, 0.6412(2))	1			
								2d (0, 0, 0.1350)	0.8Co + 0.2Ni			

M1 = 0.1Co + 0.9 Ni; M2 = 0.466Co + 0.534Ni; M3 = 0.438Co + 0.562Ni; M4 = 0.8Co + 0.2Ni

### 3.4.2. Crystal Structure of $\text{Co}_{1-x}\text{Ni}_x\text{In}_2$ ( $x = 0.540, 0.580$ )

A large difference in the melting points of Co, Ni, and In (Co:1768K, Ni:1726K, In:429K) [37,38] causes difficulty in obtaining good single-phase  $\text{Co}_{1-x}\text{Ni}_x\text{In}_2$  samples. Thus, the crystal structure of  $\text{Co}_{1-x}\text{Ni}_x\text{In}_2$  was investigated with a few selected good single-phase samples. The crystal structure of  $\text{Co}_{1-x}\text{Ni}_x\text{In}_2$  ( $x = 0.540, 0.580$ ) at 673 K was investigated via XRD and SEM/EDS. Figures 16 and 17 present the XRD patterns of  $\text{Co}_{1-x}\text{Ni}_x\text{In}_2$ . Table 4 lists the Rietveld refinement results of  $\text{Co}_{1-x}\text{Ni}_x\text{In}_2$ . The lower values of  $R_p$  and  $R_{wp}$  for the Rietveld refinement indicate that the refinement results are credible. The SEM/EDS results show that the composition of  $\text{Co}_{1-x}\text{Ni}_x\text{In}_2$  ( $x = 0.580$ ) is Co16.97(4)Ni18.02 (5)In65.01(5); see Table S1. The refinement result shows that the  $\text{Co}_{1-x}\text{Ni}_x\text{In}_2$  ( $x = 0.540$ ) compound, in which a large number of Co atoms are replaced by Ni, remains in the single phase and maintains the  $\text{Cu}_2\text{Mg}$ -type structure with the space group  $Fddd$  (No. 70). The lattice parameters of  $\text{Co}_{1-x}\text{Ni}_x\text{In}_2$  ( $x = 0.540$ ) are refined to be  $a = 0.9424(3)$  nm,  $b = 0.5288(4)$  nm, and  $c = 1.7742(5)$  nm. The  $\text{Co}_{1-x}\text{Ni}_x\text{In}_2$  ( $x = 0.580$ ) alloy contains the  $\text{Co}_{1-x}\text{Ni}_x\text{In}_2$  ( $x = 0.565$ ) ( $\text{Cu}_2\text{Mg}$ -type structure) phase with a small amount of the  $\text{Ni}_{2-x}\text{Co}_x\text{In}_3$  ( $x = 0.400$ ) ( $\text{Al}_3\text{Ni}_2$ -type structure). The EDS results shows that the compositions of the  $\text{Co}_{1-x}\text{Ni}_x\text{In}_2$  ( $x = 0.565$ ) and  $\text{Ni}_{2-x}\text{Co}_x\text{In}_3$  ( $x = 0.400$ ) phases were about Co14.11(4)Ni18.64(3)In67.25(4) and Co7.41(3)Ni35.27(4)In57.3(4)2, which were identified as  $\text{Co}_{1-x}\text{Ni}_x\text{In}_2$  ( $x = 0.565$ ) and  $\text{Ni}_{2-x}\text{Co}_x\text{In}_3$  ( $x = 0.400$ ), respectively. This also proves that the solubility of Ni in  $\text{Co}_{1-x}\text{Ni}_x\text{In}_2$  is 18.64 at.% Ni in the  $\text{Ni}_{2-x}\text{Co}_x\text{In}_3$  ( $x = 0.400$ ) alloy. The Rietveld refinement of the  $\text{Co}_{1-x}\text{Ni}_x\text{In}_2$  ( $x = 0.580$ ) alloy shows that the mass fractions of these two phases in the sample were 2.7% and 97.3 %, respectively. The Rietveld refinement also indicated that the amount of Ni in the phase of  $\text{Co}_{1-x}\text{Ni}_x\text{In}_2$  was  $x = 0.565$ . This is in agreement with the results of solid solubility determination including the SEM/EDS measurements. The refined lattice parameters of  $\text{Co}_{1-x}\text{Ni}_x\text{In}_2$  ( $x = 0.565$ ) are  $a = 0.9421(2)$  nm,  $b = 0.5282(3)$  nm, and  $c = 1.7739(3)$  nm, which are slightly smaller than those of  $\text{Co}_{1-x}\text{Ni}_x\text{In}_2$  ( $x = 0.540$ ). This phenomenon is mainly due to the similar crystal structure of Co and Ni, and the radius of Ni ( $R_{\text{Ni}} = 0.124$  nm) atom is slightly smaller than that of Co ( $R_{\text{Co}} = 0.125$  nm). The replacement of Ni atoms for Co atoms causes the volume of  $\text{Co}_{1-x}\text{Ni}_x\text{In}_2$  to shrink. This results in smaller sizes. The lattice parameters of  $\text{Ni}_{2-x}\text{Co}_x\text{In}_3$  ( $x = 0.400$ ) are refined to be  $a = 0.4397(1)$  nm and  $0.5319(3)$  nm. In the structure of  $\text{Co}_{1-x}\text{Ni}_x\text{In}_2$ , the In atoms occupy the 16e and 16g sites, while Co atoms (including the substituting Ni atoms) exist at the 16g sites.

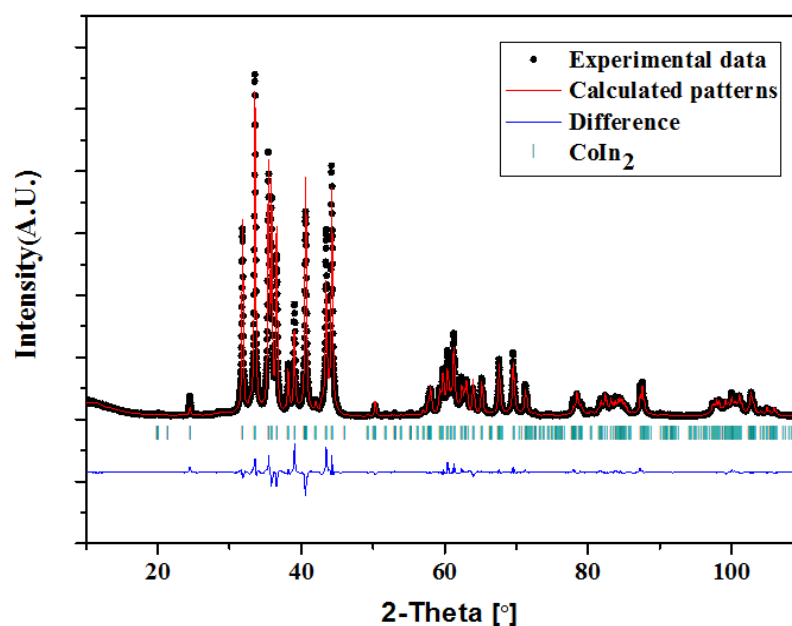


Figure 16. Observed, calculated and differential XRD patterns of  $\text{Co}_{1-x}\text{Ni}_x\text{In}_2$  ( $x = 0.540$ ).

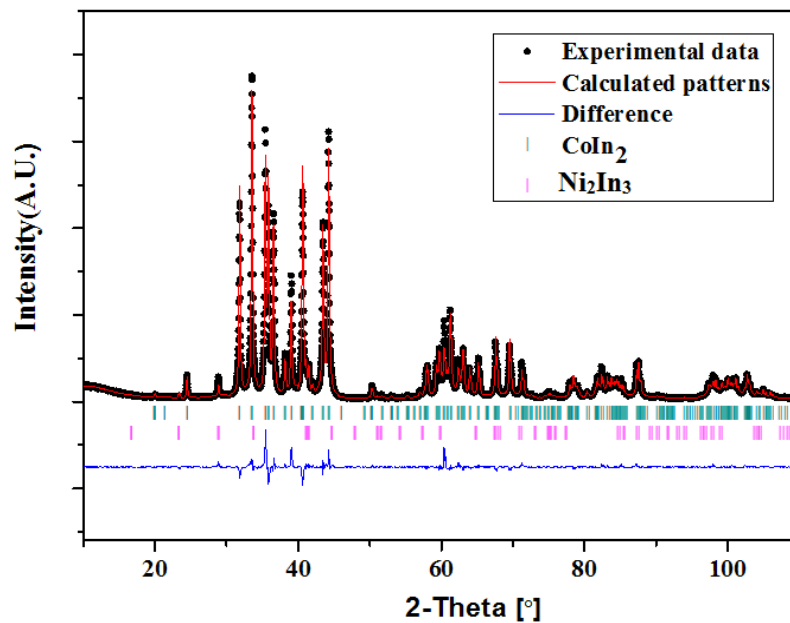


Figure 17. Observed, calculated and differential XRD patterns of  $\text{Co}_{1-x}\text{Ni}_x\text{In}_2$  ( $x = 0.580$ ).

### 3.5. Magnetic Properties

#### 3.5.1. Magnetic Properties of $\text{Ni}_{2-x}\text{Co}_x\text{In}_3$ ( $x = 0.200$ )

Figure 18 shows the zero-field-cooled (ZFC) and zero-field-heated (ZFH) temperature dependence of the magnetization under a static magnetic field of 50 mT for the  $\text{Ni}_{2-x}\text{Co}_x\text{In}_3$  ( $x = 0.200$ ) alloy. During the heating process, the magnetization of the alloy remains constant at  $0.044 \text{ emu/g}$  in the range of 5–436 K, and then increases sharply at 436 K ( $T_{\text{HS}}$ ) and rises to  $1.05 \text{ emu/g}$  at 451 K ( $T_{\text{HF}}$ ). After that, the magnetization increases slowly and reaches a maximum of  $1.11 \text{ emu/g}$  at 482 K. When the temperature increases from 482 to 528 K, the magnetization slowly drops to  $1.05 \text{ emu/g}$ . The magnetization drops rapidly to a minimum value of  $0.046 \text{ emu/g}$  with a further temperature increase to 560 K. The cooling curve almost completely coincides with the heating one, except in the temperature range of 339–451 K. In the cooling curve, the magnetization starts to decrease at 446 K ( $T_{\text{CS}}$ ) and stops to decrease at 399 K ( $T_{\text{CF}}$ ). The temperature cooling curve shifts to the low-temperature direction, indicating that the sample has thermal hysteresis in this temperature range;  $\Delta = 21 \text{ K}$  ( $\Delta T_{\text{hys}} = (T_{\text{HS}} + T_{\text{HF}} - T_{\text{CS}} - T_{\text{CF}})/2$ ). This is very similar to the martensitic transformation phenomenon occurring in the Ni-Mn-A ( $A = \text{Ga}, \text{Sn}, \text{In}$ ) [39–41] systems. As can be seen from the inset of Figure 18, the differential of magnetization to temperature varies with temperature and shows that the Curie temperature of the compound is 550 K.

Magnetization isotherms, measured during heating cycles at different temperatures, are shown in Figure 19. The samples show ferromagnetism at all measuring temperatures. Clearly, the magnetization increases with the increase in temperature. The magnetization increases from  $0.178 \text{ emu/g}$  to  $3.84 \text{ emu/g}$  when temperature is heated from 430 K to 454 K under the 3 T magnetic field. The sample has weak magnetism at 600 K—the magnetization is only  $0.147$  at 3 T. Magnetic entropy change ( $\Delta S_{\text{M}}$ ) in the system, due to the application of external magnetic field, can be determined from Maxwell's relation (Equation (1)) by integrating the magnetization isotherms over the magnetic field.

$$\Delta S_{\text{M}}(T, H_{\text{max}}) = S_{\text{M}}(T, H_{\text{max}}) - S_{\text{M}}(T, 0) = \int_0^{H_{\text{max}}} \left( \frac{\partial M}{\partial H} \right)_H dH \quad (1)$$

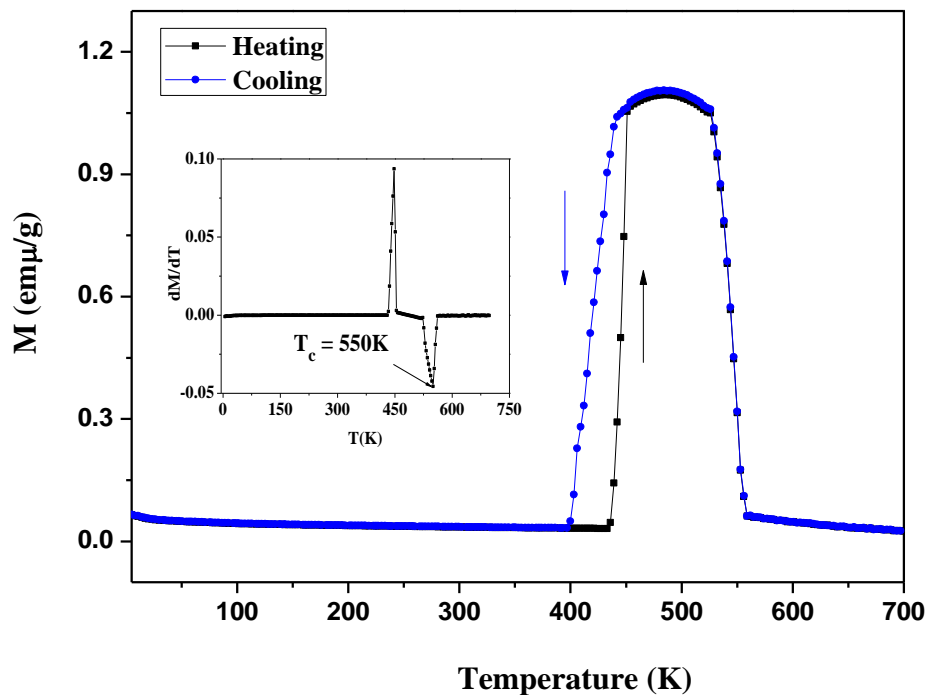


**Figure 18.** The zero-field-cooled (ZFC) and zero-field-heated (ZFH) temperature dependence of the magnetization under static magnetic fields of 50 mT for the  $\text{Ni}_{2-x}\text{Co}_x\text{In}_3$  ( $x = 0.200$ ) alloy.

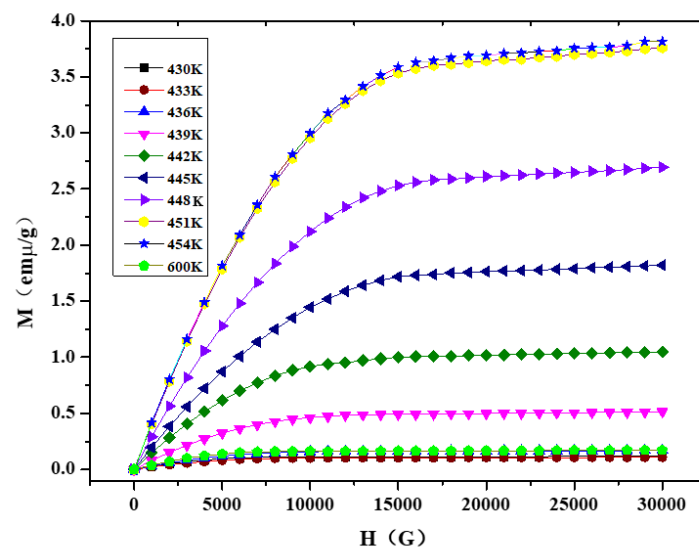


**Figure 19.** Magnetization isotherms of the  $\text{Ni}_{2-x}\text{Co}_x\text{In}_3$  ( $x = 0.200$ ) alloy.

Magnetic entropy changes in the alloy have been derived from the isothermal magnetization curves. Figure 20 shows the magnetic entropy change in the  $\text{Ni}_{2-x}\text{Co}_x\text{In}_3$  ( $x = 0.200$ ) sample as a function of temperature near 445 K under the 3 T, 2 T, and 1 T magnetic fields. Clearly, the greater the magnetic entropy, the stronger the magnetic field. The peak value under a field change of 3 T is  $1.25 \text{ J kg}^{-1}\text{K}^{-1}$  at  $T = 449.5 \text{ K}$ . The relative cooling power ( $R_{\text{CP}} = \Delta S_{\text{M}} \times \Delta T_{\text{FWHM}}$ ), which is the measure of the amount of heat transfer between the cold and hot reservoirs in an ideal refrigeration cycle, is evaluated to be  $14.125 \text{ J kg}^{-1}\text{K}^{-1}$  in the vicinity of 430–454 K for 3 T magnetic field change, where  $\Delta T_{\text{FWHM}} = 11.3 \text{ K}$ .

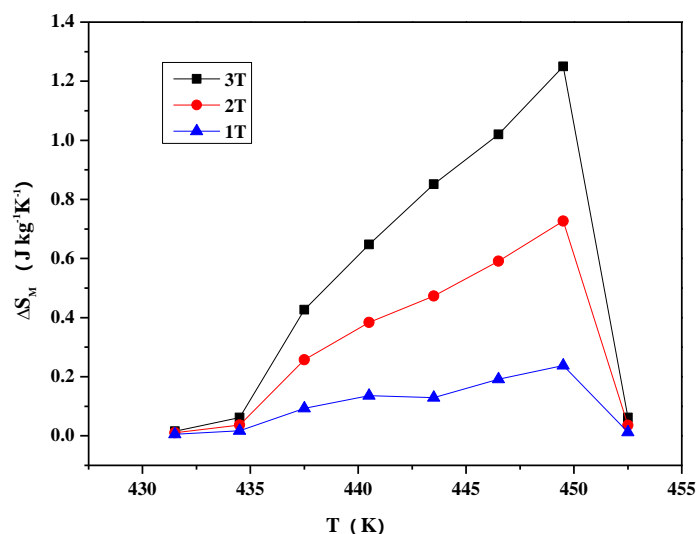
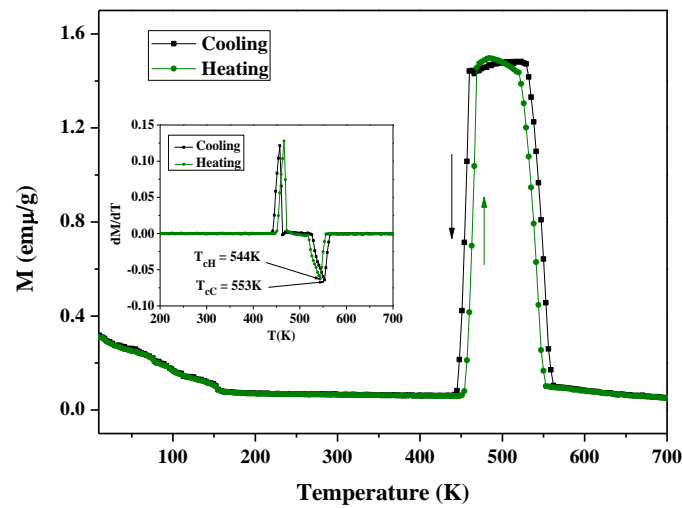


**Figure 20.** The magnetic entropy changes as a function of temperature under 3 T, 2 T, 1 T magnetic fields for the  $\text{Ni}_{2-x}\text{Co}_x\text{In}_3$  ( $x = 0.200$ ) alloy.

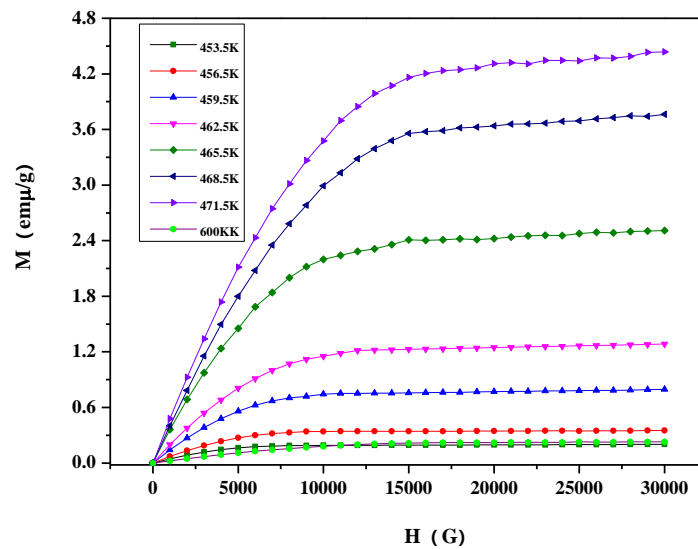
### 3.5.2. Magnetic Properties of $\text{Co}_{1-x}\text{Ni}_x\text{In}_2$ ( $x = 0.540$ )

Figure 21 shows the magnetization behavior of the  $\text{Co}_{1-x}\text{Ni}_x\text{In}_2$  ( $x = 0.540$ ) alloy during thermal cycling with a heating/cooling rate of 5 K/min at ZFC and ZFH. The tendency of magnetization changes with temperature of the  $\text{Co}_{1-x}\text{Ni}_x\text{In}_2$  ( $x = 0.540$ ) compound is very similar to that of  $\text{Ni}_{2-x}\text{Co}_x\text{In}_3$  ( $x = 0.200$ ). However, there are two hysteresis taking place in the  $\text{Co}_{1-x}\text{Ni}_x\text{In}_2$  ( $x = 0.540$ ) alloy. The  $\Delta T_{\text{hys}}$  in low temperature is 8.5 K, which is smaller than  $\text{Ni}_{2-x}\text{Co}_x\text{In}_3$  ( $x = 0.200$ ). As can be seen from the inset of Figure 21, due to the thermal hysteresis, two different Curie temperatures (544 K and 553 K) can be obtained from the heating curve and the cooling curve. Representative isothermal magnetization loops measured around 462.5 K for  $\text{Co}_{1-x}\text{Ni}_x\text{In}_2$  ( $x = 0.540$ ) are presented in Figure 22. The sample shows a low magnetization below 459 K, which rises from 0.21 emu/g to 4.46 emu/g with a temperature increase from 453 K to 471 K at the magnetic field of 3T. Associated with this magnetostructural transition, a large magnetic entropy change occurs. Figure 23 shows the magnetic entropy change as a function of temperature under the 3 T, 2 T, and 1 T magnetic fields for the alloy. It is clearly seen that as the magnetic field increases, the magnetic entropy of the  $\text{Co}_{1-x}\text{Ni}_x\text{In}_2$  ( $x = 0.540$ ) compound becomes larger. Under a magnetic field of 3 T, the magnetic entropy of the alloy reaches a maximum of  $1.475 \text{ J kg}^{-1} \text{ K}^{-1}$  at about 463.5 K. The corresponding half-maximum width is  $\Delta T_{\text{FWHM}} = 8.9 \text{ K}$  for the compound. The direct  $R_{\text{CP}}$  is evaluated as  $13.128 \text{ J kg}^{-1} \text{ K}^{-1}$ .

Since the magnetization dependence of temperature (MT) curves of  $\text{Ni}_{2-x}\text{Co}_x\text{In}_3$  ( $x = 0.200$ ) and  $\text{Co}_{1-x}\text{Ni}_x\text{In}_2$  ( $x = 0.540$ ) are similar to those of ferromagnetic shape memory alloys with martensitic transformation, temperature-dependent powder XRD measurements were performed in order to obtain further insights into whether the compound undergoes martensite transformation behavior. Figure 24 shows the XRD patterns for the  $\text{Ni}_{2-x}\text{Co}_x\text{In}_3$  ( $x = 0.200$ ) alloy measured at 490 K. According to XRD patterns, the main phase of the alloy at 490 K still was a  $\text{Ni}_2\text{In}_3$  phase with an  $\text{Al}_2\text{Ni}_3$ -type structure. Furthermore, a small amount of  $\text{Ni}_{10}\text{In}_{27}$  (space group  $\text{Im-3 m}$ ) and  $\text{Ni}_2\text{In}$  (space group  $\text{P63/mmc}$ ) appears in alloy. The results indicate that a small amount of  $\text{Ni}_{10}\text{In}_{27}$  and  $\text{Ni}_2\text{In}$  is generated during heating. Indexing of the  $\text{Ni}_2\text{In}_3$  phase showed that  $a = 0.43905$  (5) nm,  $c = 0.52930$  (3) nm, and  $V = 0.08836 \text{ nm}^3$ . All these results show that a structure phase transformation but not a martensitic transformation occurred in  $\text{Ni}_{2-x}\text{Co}_x\text{In}_3$  ( $x = 0.200$ ) during heating. Figure 25 shows the XRD patterns of the  $\text{Co}_{1-x}\text{Ni}_x\text{In}_2$  ( $x = 0.540$ ) alloy at 490 K, which still retains the  $\text{Cu}_2\text{Mg}$ -type structure type at 490 K. These results point to the notion that no martensitic transformation occurred in the  $\text{Co}_{1-x}\text{Ni}_x\text{In}_2$  ( $x = 0.540$ ) alloys during heating.



**Figure 21.** The ZFC and ZFH temperature dependence of the magnetization under static magnetic fields of 50 mT for the  $\text{Co}_{1-x}\text{Ni}_x\text{In}_2$  ( $x = 0.540$ ) compound.



**Figure 22.** Magnetization isotherms for the  $\text{Co}_{1-x}\text{Ni}_x\text{In}_2$  ( $x = 0.540$ ) alloy.

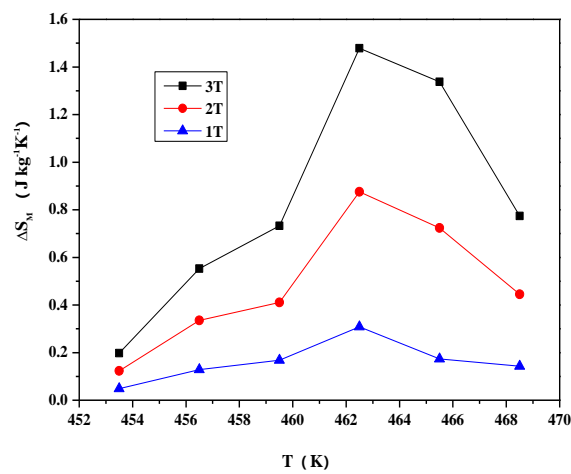


**Figure 23.** The magnetic entropy changes as a function of temperature under 3 T, 2 T, and 1 T magnetic fields for the  $\text{Co}_{1-x}\text{Ni}_x\text{In}_2$  ( $x = 0.540$ ) alloy.

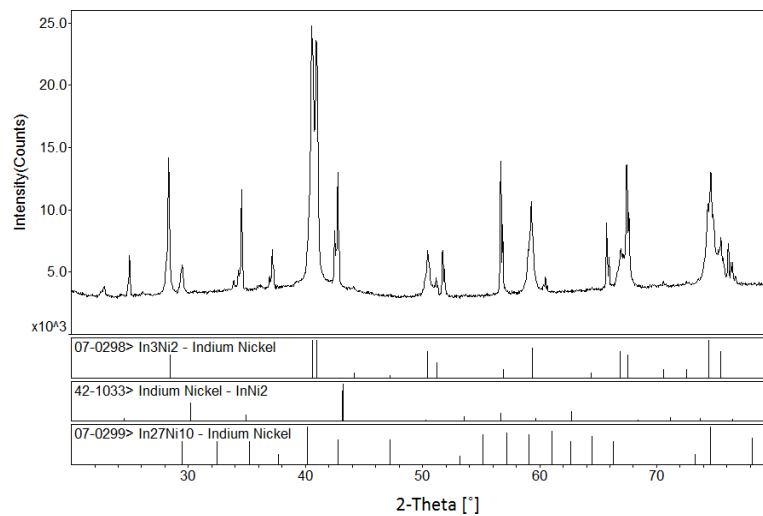


**Figure 24.** The XRD patterns of sample  $\text{Ni}_{2-x}\text{Co}_x\text{In}_3$  ( $x = 0.200$ ) at 490 K.

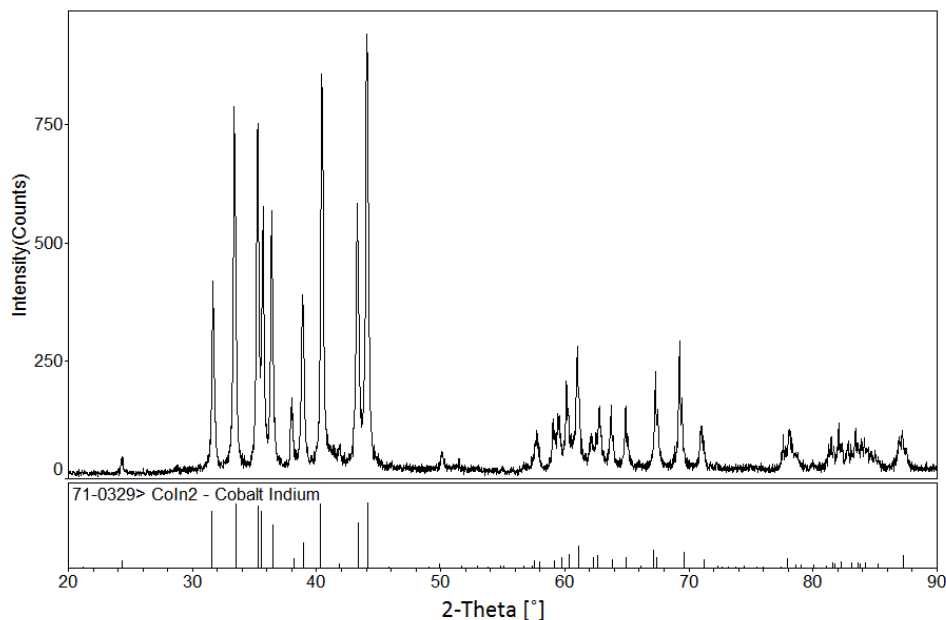


**Figure 25.** The XRD patterns of sample  $\text{Co}_{1-x}\text{Ni}_x\text{In}_2$  ( $x = 0.540$ ) at 490 K.

#### 4. Conclusions

More than 130 samples were prepared and investigated by experimental methods to establish the phase equilibrium of the ternary Co-Ni-In system at 673 K and 873 K. The peculiar MT curves of  $\text{Ni}_{2-x}\text{Co}_x\text{In}_3$  ( $x = 0.200$ ) and  $\text{Co}_{1-x}\text{Ni}_x\text{In}_2$  ( $x = 0.540$ ) allow them to have potential to become magnetic functional materials.

1. There are eight Co-Ni-In binary compounds existing at 673 K and six binary compounds existing at 873 K. Compared to the phases at 673 K, the binary compounds  $\text{Ni}_3\text{In}_7$ ,  $\text{CoIn}_3$ , and  $\text{CoIn}_2$  disappeared, and  $\xi$  exists at 873 K.
2. The solid solubility range of  $\text{Co}_{1-x}\text{Ni}_x\text{In}_2$  was found to be 0–18.64% at. % Ni at 673 K, while it shifted to the range of 3–20.1% at. % Ni at 873 K due to the absence of  $\text{CoIn}_2$  at 873 K.
3. The isothermal section of the phase diagram of the Co-Ni-In system at 673 K consists of 11 single-phase regions, 21 two-phase regions, and 9 three-phase regions, and the isothermal section at 873 K contains 8 single-phase regions, 16 two-phase regions, and 8 three-phase regions.

Three-phase regions disappear due to the absence of the binary compounds  $\text{Ni}_3\text{In}_7$  and  $\text{CoIn}_3$  at 873 K. The three-phase region  $\text{Ni}_{13-x}\text{Co}_x\text{In}_9$  ( $x = 0.702$ ) +  $\text{Ni}_{1-x}\text{Co}_x\text{In}_2$  ( $x = 0.091$ ) +  $\alpha\text{-Ni}_{1-x}\text{Co}_x$  ( $x = 0.400$ ) breaks into two three-phase regions due to the  $\xi$  phase existing at 873 K.

- The MT curves of  $\text{Ni}_{2-x}\text{Co}_x\text{In}_3$  ( $x = 0.200$ ) and  $\text{Co}_{1-x}\text{Ni}_x\text{In}_2$  ( $x = 0.540$ ), which are similar to the Ni-Mn-A ( $A = \text{Ga}, \text{Sn}, \text{In}$ ), do not undergo martensitic transformation at temperatures, which results in a sharp change in magnetization. The maximum magnetic entropy changes of  $\text{Ni}_{2-x}\text{Co}_x\text{In}_3$  ( $x = 0.200$ ) and  $\text{Co}_{1-x}\text{Ni}_x\text{In}_2$  ( $x = 0.540$ ) under 3T in 430 K–454 K and 454 K–472 K are  $1.25 \text{ J kg}^{-1}\text{K}^{-1}$ ,  $1.475 \text{ J kg}^{-1}\text{K}^{-1}$ , respectively.

**Supplementary Materials:** The following are available online at <http://www.mdpi.com/1996-1944/13/18/3990/s1>, Table S1: XRD and SEM/EDS analysis results of the selected Co-Ni-In samples at 673 K, Table S2: XRD and SEM/EDS analysis results of the selected Co-Ni-In samples at 873 K.

**Author Contributions:** W.H.: project administration, investigation, writing—review and editing. T.Y.: investigation, writing, data curation. G.C.: investigation, Software. W.Z.: investigation, methodology. J.W.: investigation. L.Z.: formal analysis. J.L.: investigation, visualization. All authors have read and agreed to the published version of the manuscript.

**Funding:** This work was jointly supported by the National Natural Science Foundation of China (Nos. 51861003 & 51461004).

**Conflicts of Interest:** The authors declare no conflict of interest.

## References

- Imano, Y.; Ito, W.; Sutou, Y.; Morito, H.; Okamoto, S.; Kitakami, O.; Oikawa, K.; Fujita, A.; Kanomata, T.; Ishida, K. Magnetic-field-induced shape recovery by reverse phase transformation. *Nature* **2006**, *439*, 957–960.
- Liu, J.; Gottschall, T.; Skokov, K.P.; James, D.M.; Oliver, G. Giant magnetocaloric effect driven by structural transitions. *Nat. Mater.* **2012**, *11*, 620–626. [[CrossRef](#)]
- Bonnot, E.; Romero, R.; Manosa, L.; Vives, E.; Planes, A. Elastocaloric effect associated with the martensitic transition in shape-memory alloys. *Phys. Rev. Lett.* **2008**, *100*, 125901. [[CrossRef](#)]
- Zhang, B.; Zhang, X.X.; Yu, S.Y.; Chen, J.L.; Cao, Z.X.; Wu, G.H. Giant magnetothermal conductivity in the Ni-Mn-In ferromagnetic shape memory alloys. *Appl. Phys. Lett.* **2007**, *91*, 012510. [[CrossRef](#)]
- Krenke, T.; Duman, E.; Acet, M.; Wassermann, E.F. Magnetic superelasticity and inverse magnetocaloric effect in Ni-Mn-In. *Phys. Rev. B* **2007**, *75*, 104414. [[CrossRef](#)]
- Mañosa, L.; González-Alonso, D.; Planes, A.; Bonnot, E.; Barrio, M.; Tamarit, J.; Aksoy, S.; Acet, M. Giant solid-state barocaloric effect in the Ni-Mn-In magnetic shape-memory alloy. *Nat. Mater.* **2010**, *9*, 478–481. [[CrossRef](#)]
- Wang, B.M.; Liu, Y.; Ren, P.; Xia, B.; Ruan, K.B.; Yi, J.B.; Ding, J.; Li, X.G.; Wang, L. Large Exchange Bias after Zero-Field Cooling from an Unmagnetized State. *Phys. Rev. Lett.* **2011**, *106*, 077203. [[CrossRef](#)]
- Ito, W.; Imano, Y.; Kainuma, R.; Sutou, Y.; Oikawa, K.; Ishida, K. Martensitic and Magnetic Transformation Behaviors in Heusler-Type NiMnIn and NiCoMnIn Metamagnetic Shape Memory Alloys. *Metall. Mater. Trans.* **2007**, *38*, 759–766. [[CrossRef](#)]
- Wu, Z.G.; Liu, Z.H.; Yang, H.; Liu, Y.N.; Wu, G.H. Metamagnetic phase transformation in  $\text{Mn}_{50}\text{Ni}_{37}\text{In}_{10}\text{Co}_3$  polycrystalline alloy. *Appl. Phys. Lett.* **2011**, *98*, 061904. [[CrossRef](#)]
- Wu, Z.G.; Liu, Z.H.; Yang, H.; Liu, Y.N.; Wu, G.H. Effect of Co addition on martensitic phase transformation and magnetic properties of  $\text{Mn}_{50}\text{Ni}_{40-x}\text{In}_{10}\text{Co}_x$  polycrystalline alloys. *Intermetallics* **2011**, *19*, 1839–1848. [[CrossRef](#)]
- He, X.J.; Wei, S.X.; Kang, Y.R.; Zhang, Y.L.; Cao, Y.M.; Xu, K.; Li, Z.; Jing, C. Enhanced barocaloric effect produced by hydrostatic pressure-induced martensitic transformation for  $\text{Ni}_{44.6}\text{Co}_{5.5}\text{Mn}_{35.5}\text{In}_{14.4}$  Heusler alloy. *Scr. Mater.* **2018**, *145*, 58–61. [[CrossRef](#)]
- Zhang, X.X.; Qian, M.F.; Miao, S.P.; Su, R.Z.; Liu, Y.F.; Geng, L.; Sun, J.F. Enhanced magnetic entropy change and working temperature interval in Ni-Mn-In-Co alloys. *J. Alloys Compd.* **2016**, *656*, 154–158. [[CrossRef](#)]
- Monroe, J.A.; Karaman, I.; Basaran, B.; Ito, W.; Umetsu, R.Y.; Kainuma, R.; Koyama, K.; Chumlyakov, Y.I. Direct measurement of large reversible magnetic-field-induced strain in Ni-Co-Mn-In metamagnetic shape memory alloys. *Acta Mater.* **2012**, *60*, 6883–6891. [[CrossRef](#)]

14. Liu, J.; Aksoy, S.; Scheerbaum, N.; Acet, M.; Gutfleisch, O. Large magnetostrain in polycrystalline Ni-Mn-In-Co. *Appl. Phys. Lett.* **2009**, *95*, 232515.
15. Madiligama, A.S.B.; Ari-Gur, P.; Shavrov, V.G.; Koledov, V.V.; Calder, S.; Mashirov, A.V.; Kamantsev, A.P.; Dilmieva, E.T.; Gonzalez-Legarreta, L.; Grande, B.H.; et al. Crystalline structure and magnetic behavior of the Ni<sub>41</sub>Mn<sub>39</sub>In<sub>12</sub>Co<sub>8</sub> alloy demonstrating giant magnetocaloric effect. *Smart Mater. Struct.* **2016**, *25*, 085013. [[CrossRef](#)]
16. Gottschall, T.; Skokov, K.P.; Frincu, B.; Gutfleisch, O. Large reversible magnetocaloric effect in Ni-Mn-In-Co. *Appl. Phys. Lett.* **2015**, *106*, 021901. [[CrossRef](#)]
17. Huang, L.; Cong, D.Y.; Ma, L.; Nie, Z.H.; Wang, Z.L.; Suo, H.L.; Ren, Y.; Wang, Y.D. Large reversible magnetocaloric effect in a Ni-Co-Mn-In magnetic shape memory alloy. *Appl. Phys. Lett.* **2016**, *108*, 032405. [[CrossRef](#)]
18. Cheng, F.; Gao, L.M.; Wang, Y.; Wang, J.T.; Liao, X.Q.; Yang, S. Large refrigeration capacity in a Ni<sub>42</sub>Co<sub>8</sub>Mn<sub>37.7</sub>In<sub>12.3</sub> magnetocaloric alloy. *J. Magn. Magn. Mater.* **2019**, *478*, 234–238. [[CrossRef](#)]
19. Karaca, H.E.; Karaman, I.; Basaran, B.; Ren, Y.; Chumlyakov, Y.I.; Maier, H.J. Magnetic Field-Induced Phase Transformation in NiMnCoIn Magnetic Shape-Memory Alloys—A New Actuation Mechanism with Large Work Output. *Adv. Funct. Mater.* **2009**, *19*, 983–998. [[CrossRef](#)]
20. Wang, Y.D.; Huang, E.W.; Ren, Y.; Nie, Z.H.; Wang, G.; Liu, Y.D.; Deng, J.N.; Choo, H.; Liaw, P.K.; Brown, D.E.; et al. In situ high-energy X-ray studies of magnetic-field-induced phase transition in a ferromagnetic shape memory Ni-Co-Mn-In alloy. *Acta Mater.* **2008**, *56*, 913–923. [[CrossRef](#)]
21. Pérez-Landazábal, J.I.; Recarte, V.; Sánchez-Alarcos, V.; Gómez-Polo, C.; Kustov, S.; Cesari, E. Magnetic field induced martensitic transformation linked to the arrested austenite in a Ni-Mn-In-Co shape memory alloy. *Appl. Phys. Lett.* **2011**, *109*, 093515. [[CrossRef](#)]
22. Feng, Y.; Chen, H.; Xiao, F.; Bian, X.H.; Wang, P. Improvement of mechanical property and large shape recovery of sintered Ni<sub>45</sub>Mn<sub>36.6</sub>In<sub>13.4</sub>Co<sub>5</sub> alloy. *J. Alloys Compd.* **2018**, *765*, 264–270. [[CrossRef](#)]
23. Madiligama, A.; Ari-Gur, P.; Ren, Y.; Koledov, V.V.; Dilmieva, E.T.; Kamantsev, A.P.; Mashirov, A.V.; Shavrov, V.G.; Gonzalez-Legarreta, L.; Grande, B.H. Thermal and magnetic hysteresis associated with martensitic and magnetic phase transformations in Ni<sub>52</sub>Mn<sub>25</sub>In<sub>16</sub>Co<sub>7</sub> Heusler alloy. *J. Magn. Magn. Mater.* **2017**, *442*, 25–35. [[CrossRef](#)]
24. Turabi, A.S.; Karaca, H.E.; Tobe, H.; Basaran, B.; Aydogdu, Y.; Chumlyakov, Y.I. Shape memory effect and superelasticity of NiMnCoIn metamagnetic shape memory alloys under high magnetic field. *Scr. Mater.* **2016**, *111*, 110–113. [[CrossRef](#)]
25. Ao, W.Q.; Liu, F.S.; Li, J.Q.; Du, Y.; Liu, F.L. Isothermal section of the Ni-Mn-In ternary system at 773 K. *J. Alloys Compd.* **2015**, *622*, 149–154. [[CrossRef](#)]
26. Miyamoto, T.; Nagasako, M.; Kainuma, R. Phase equilibria in the Ni-Mn-In alloy system. *J. Alloys Compd.* **2013**, *549*, 57–63. [[CrossRef](#)]
27. Gupta, K.P. The Co-Mn-Ni (Cobalt-Manganese-Nickel) system. *J. Phase Equilib.* **1999**, *20*, 527–532. [[CrossRef](#)]
28. Zhou, Y.; Nash, P.; Dai, X.; Li, D.; Silva, A.; Cardoso, G. Phase equilibria in the Co-Mn-Ni system. *J. Alloys Compd.* **2018**, *777*, 1274–1285. [[CrossRef](#)]
29. Nash, P.; Nash, A. *Phase Diagrams of Binary Nickel Alloy*; ASM International: Materials Park, OH, USA, 1991; p. 229.
30. Okamoto, H. Co-In. *J. Phase Equilib. Diffus.* **1997**, *18*, 3.
31. Durussel, P.; Burri, G.; Feschotte, E. The binary system Ni-In. *J. Alloys Compd.* **1997**, *257*, 253–258. [[CrossRef](#)]
32. Bai, J.; Xu, N.; Raulot, J.M.; Zhang, Y.D.; Esling, C. First-principles investigations of crystallographic, magnetic, and electronic structures in Ni<sub>2</sub>XIn (X = Mn, Fe, and Co). *Appl. Phys.* **2012**, *112*, 114901. [[CrossRef](#)]
33. Villars, P. *Pearson's Handbook, Desk Edition: Crystallographic Data for Intermetallic Phases*; ASM International: Materials Park, OH, USA, 1997; p. 1.
34. Roisnel, T.; Rodriguez-Carvajal, J. WinPLOTR: A windows tool for powder diffraction patterns analysis. *Mater. Sci.* **2001**, *378–381*, 118–123. [[CrossRef](#)]
35. Rodriguez-Carvajal, J. Recent advances in magnetic structure determination by neutron powder diffraction. *Physica B* **1993**, *192*, 55–69. [[CrossRef](#)]
36. Schmetterer, C.; Zemanova, A.; Flandorfer, H. Phase equilibria in the ternary In-Ni-Sn system at 700 °C. *Intermetallics* **2013**, *35*, 90–94. [[CrossRef](#)] [[PubMed](#)]

37. Howe, R.A.; Enderby, J.E. The thermoelectric power of cerium, lanthanum, nickel and cobalt in the vicinity of the melting point. *J. Phys. F Met. Phys.* **1973**, *3*, 12–14. [[CrossRef](#)]
38. Maira, G.K.; Orton, B.R.; Riviere, J.C. An XPS study of indium through the melting point. *J. Phys. F Met. Phys.* **1987**, *17*, 10. [[CrossRef](#)]
39. Seguí, C.; Cesari, E.; Pons, J. Intermartensitic Transformations in Ni-Mn-Ga Alloys: A General View. *Adv. Mater. Res.* **2008**, *52*, 47–55. [[CrossRef](#)]
40. Krenke, T.; Acet, M.; Wassermann, E.F. Ferromagnetism in the austenitic and martensitic states of Ni-Mn-In alloys. *Phys. Rev. B* **2006**, *7*, 174413. [[CrossRef](#)]
41. Krenke, T.; Acet, M.; Wassermann, E.F. Martensitic transitions and the nature of ferromagnetism in the austenitic and martensitic states of Ni-Mn-Sn alloys. *Phys. Rev. B* **2005**, *72*, 014412. [[CrossRef](#)]



© 2020 by the authors. Licensee MDPI, Basel, Switzerland. This article is an open access article distributed under the terms and conditions of the Creative Commons Attribution (CC BY) license (<http://creativecommons.org/licenses/by/4.0/>).